Tectonics

RESEARCH ARTICLE
10.1029/2019TC005797

Key Points:
- New survey-GNSS data record gravity-driven, lateral material flow out of the Pamir Plateau and shortening of the Tajik Basin deposits
- The Vakhsh fault accommodates 15 + 4/−2 mm/yr shortening and 16 ±3 mm/yr dextral shear, the Darvaz fault ~15 mm/yr sinistral shear
- The 2015 M_w7.2 Sarez earthquake may have triggered ~2 cm of slip on the Darvaz fault reverse to its interseismic loading sense

Supporting Information:
- Supporting Information S1
- Data Set S1
- Data Set S2

Correspondence to:
S. Metzger,
metzger@gfz-potsdam.de

Citation:
Metzger, S., Ischuk, A., Deng, Z., Ratschbacher, L., Perry, M., Kufner, S.-K., et al. (2020). Dense GNSS profiles across the northwestern tip of the India-Asia collision zone: Triggered slip and westward flow of the Peter the First Range, Pamir, into the Tajik Depression. *Tectonics*, *39*, e2019TC005797. https://doi.org/10.1029/2019TC005797

Received 31 JUL 2019
Accepted 24 JAN 2020
Accepted article online 26 JAN 2020

Dense GNSS Profiles Across the Northwestern Tip of the India-Asia Collision Zone: Triggered Slip and Westward Flow of the Peter the First Range, Pamir, Into the Tajik Depression

Sabrina Metzger[1], Anatoly Ischuk[2], Zhiguo Deng[1], Lothar Ratschbacher[3], Mason Perry[4], Sofia-Katerina Kufner[1], Rebecca Bendick[4], and Marcos Moreno[5]

[1]Helmholtz-Zentrum Potsdam, Deutsches GeoForschungsZentrum, Potsdam, Germany, [2]Institute of Geology, Earthquake Engineering and Seismology, Academy of Sciences, Dushanbe, Tajikistan, [3]Geologie, TU Bergakademie Freiberg, Freiberg, Germany, [4]Department of Geosciences, University of Montana, Missoula, MT, USA, [5]Departamento de Geofísica, Universidad de Concepción, Concepción, Chile

Abstract At the northwestern tip of the India-Asia collision zone, the Pamir orocline overrides the Tajik Depression and the Tarim Basin and collides with the Tian Shan. Currently, the Pamir's northern edge exhibits localized shortening rates of 13–19 mm/yr. While the eastern Pamir and the Tarim Basin move northward nearly en block, north-south shortening decreases westward along the Pamir front into the Tajik Depression. In the northeastern Tajik Depression, the wedge-shaped crustal sliver of the Peter the First Range is squeezed between the dextral-transpressive Vakhsh and the sinistral-transpressive Darvaz faults. Global Navigation Satellite System (GNSS) data collected along two densely surveyed profiles detail the kinematics of north-south shortening and westward lateral extrusion in the northwestern Pamir. The 2016 campaign data suggest a short-duration dextral-slip activation of the Darvaz fault, which we interpret as a far-field effect triggered by the 2015, M_w7.2 Sarez, Central Pamir earthquake. 2013–2015 interseismic GNSS velocities and kinematic modeling show that the Darvaz fault zone accommodates ~15 mm/yr sinistral shear and ~10 mm/yr fault-normal extension below a locking depth of 9.0 + 0.4/−1.1 km. The Vakhsh fault shows shortening rates of 15 + 4/−2 mm/yr and dextral shear rates of 16 ±3 mm/yr. Jointly, these faults accommodate NW-SE shortening and southwestward material flow out of the Peter the First Range into the Tajik Depression. Together with seismic and geologic data, our and published geodetic surveys showcase the prolonged interaction of shortening and lateral material flow out of a plateau margin.

Plain Language Summary The Pamir Mountains, Central Asia, are the result of the northward indentation of the Indian continent into Eurasia. In average, the Pamir Plateau is ~3,000 m higher than the adjacent Tajik Depression to the west. We present time-series of high-precision point positioning data that show in great detail how the upper crust of the Pamir is flowing out into the lower lying Tajik Depression. This westward transport occurs on shallow-dipping, low-friction sedimentary layers that reach surface at the beginning of the Tian Shan Mountains further north. These sediments accommodate a total slip of around 2 cm, which is extremely high for continent-continent plate boundaries. In addition, our data observed a few centimeters of slip on the Darvaz fault that most probably was triggered by a large earthquake occurring in some 200 km distance. Such phenomena have so far rarely been observed.

1. Introduction

The Pamir at the northwestern tip of the India-Asia collision zone (Figure 1a) is a seismically active orogen, producing magnitude M6–7 earthquakes approximately every 10 years. Over the last 50 years, those occurred mainly along the Pamir's northern perimeter (Figure 1b). Seismicity in the Pamir interior is less frequent, as recorded in both long-term, global (Storchak et al., 2013) and temporary, local catalogs (Schurr et al., 2014). Modern geodetic observations show that the Pamir thrust system along the Pamir's leading edge has the highest shortening rates of the whole India-Asia collision zone, accommodating 13–19 mm/yr across a ~75 km N-S distance (Ischuk et al., 2013; Zubovich et al., 2010, 2016). This corresponds to ~50% of the total shortening rate between India and Asia (DeMets et al., 2010).

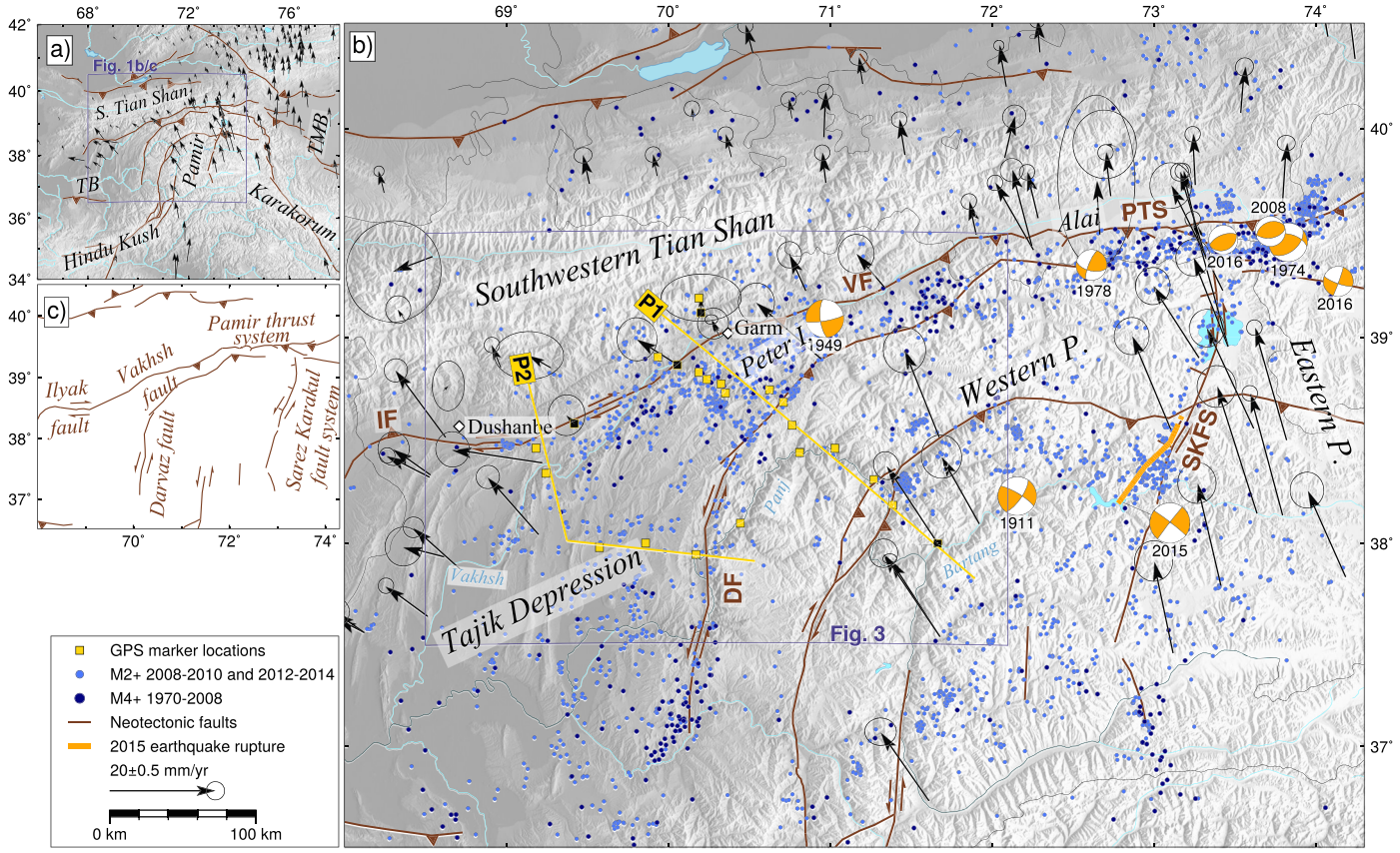

Figure 1. (a) Tectonic setting and main tectonic structures of the Pamir (in brown, Schurr et al., 2014) and published GNSS rates (Eurasia-fixed arrows, Ischuk et al., 2013; Mohadjer et al., 2010; Zubovich et al., 2010). TB = Tajik Basin; TMB = Tarim Basin. (b) Close-up of (a), highlighting the main active faults and their slip sense. (c) Close up of (a), highlighting (re)measured GNSS sites installed in 2013 (yellow squares) or earlier (black) along Profiles P1 and P2, seismicity observed by a regional network (2008–2010 and 2012–2014, bright blue, Kufner et al., 2018) and by teleseismics (1970–2008, dark blue, Engdahl et al., 1998), focal mechanisms of instrumentally recorded M6–7 earthquakes (Dziewonski et al., 1981; Ekström et al., 2012; Kulikova et al., 2015; Sippl et al., 2014) and the rupture extent of the M_w7.2 Sarez earthquake (orange line, Metzger et al., 2017). DF = Darvaz fault; VF = Vakhsh fault; PTS = Pamir thrust system; SKFS = Sarez-Karakul fault system.

The eastern Pamir, that is, the Pamir east of the Sarez-Karakul fault system, and the Tarim Basin advance toward stable Asia at nearly the same rate (Zubovich et al., 2010), allowing little shear along the eastern margin of the Pamir. In contrast, the western Pamir—west of the Sarez-Karakul fault system—moves both north and west, involving lateral extrusion (cf. Ratschbacher et al., 1991) of material from the Pamir Plateau into the Tajik Depression (Ischuk et al., 2013). The latter hosts the Tajik Basin that was inverted in the Neogene to form the thin-skinned Tajik-basin fold-thrust belt, which is detached along a basal décollement in Jurassic evaporites (Figure 1b) (e.g.,Bourgeois et al., 1997 ; Chapman et al., 2017 ; Nikolaev, 2002).

While today's shortening at the northern edge of the Pamir is mainly accommodated across the Pamir thrust system (Zubovich et al., 2010, 2016), two fault systems accommodate the more complicated relative motion between the western Pamir and southwestern Tian Shan, confining the northeastward narrowing Tajik Basin (Figure 1c): The N to NE striking, sinistral-transpressive Darvaz fault zone separates the Pamir from the Tajik Basin (Leith & Alvarez, 1985; Trifonov, 1978); the WSW striking, dextral-transpressive Vakhsh fault zone constitutes the leading thrust of the Tajik-basin fold-thrust belt in the northwestern Pamir and marks the boundary to the southwestern Tian Shan. How exactly surface motion is partitioned between these two faults is unclear (Ischuk et al., 2013). The Vakhsh fault transitions westward into the approximately east striking, dextral Ilyak fault zone (Babaev, 1975; Leith & Simpson, 1986) and continues eastward along the southern border of the Alai valley as a south dipping décollement along Jurassic evaporites (Nikolaev, 2002; Skobelev & Florenskiy, 1974). In between the Vakhsh and Darvaz fault zones, the wedge-shaped Peter the First Range hosts focused seismicity, indicating its NW-SE shortening and NE-SW lengthening (Hamburger et al., 1992; Kufner et al., 2018) (Figures 1b and 2).

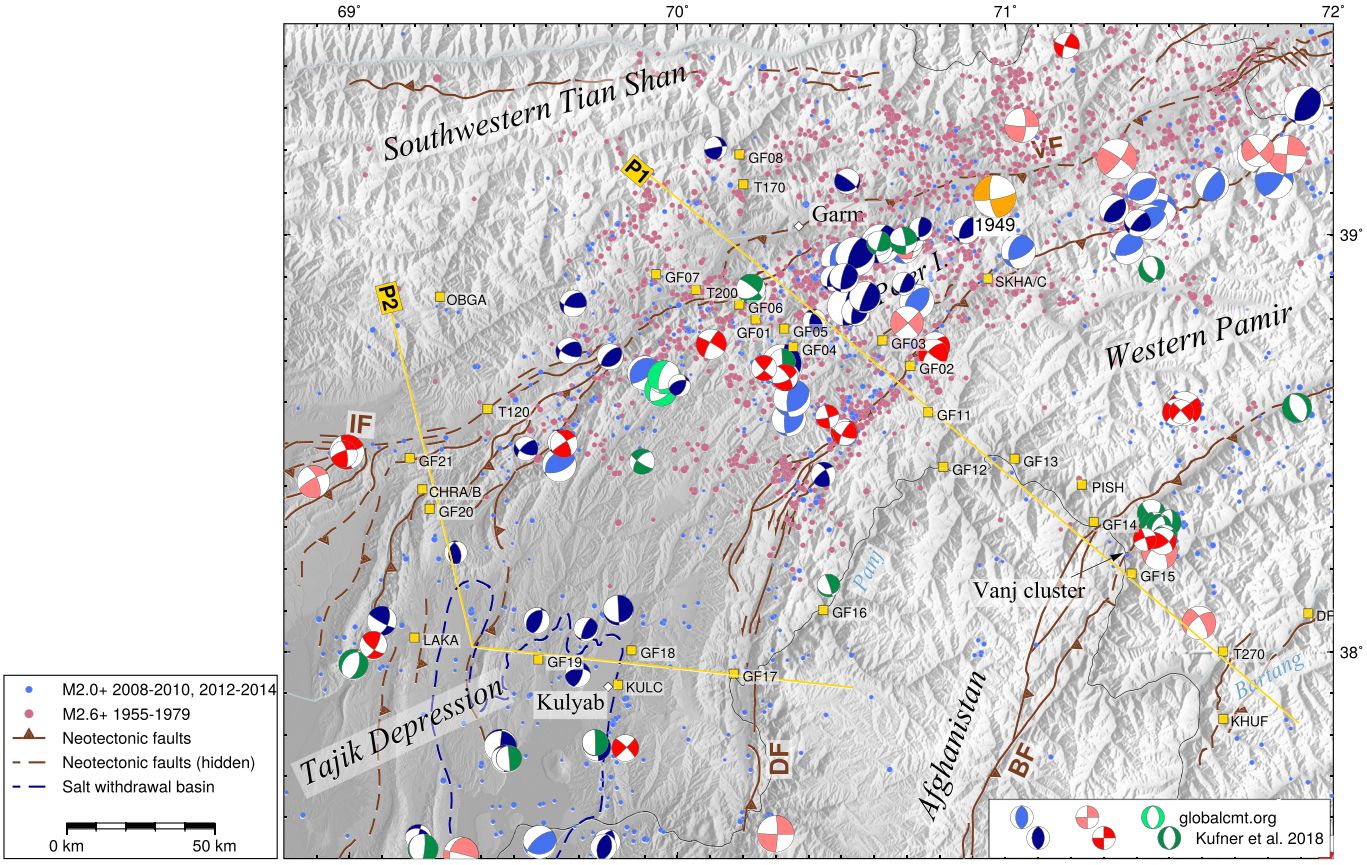

Figure 2. Seismic setting of the western Pamir, Tajik Depression, and southwestern Tian Shan. Crustal seismicity (Hamburger et al., 1992; Kufner et al., 2018), focal mechanisms (Dziewonski et al., 1981; Ekström et al., 2012; Kufner et al., 2018; Kulikova, 2016), and GNSS markers (yellow squares).

The long-term history of bulk N-S shortening and westward material flow at the northwestern Pamir-Tibet plateau margin is evident from the geologic record in the Pamir interior and shortening in the Tajik-basin fold-thrust belt (Chapman et al., 2017; Nikolaev, 2002; Rutte et al., 2017; Stübner et al., 2013; Worthington et al., 2019). Paleogene fold nappes in the Central Pamir record crustal thickening but accompanying along-strike flow lineations imply orogen-parallel material transport. Dextral wrenching and fold-axis parallel, E-W extension in upper crustal thrust sheets, and the pinch and swell geometry of the Pamir gneiss domes record Neogene orogen-parallel material transport at shallower crustal levels. Whereas currently and over most of the Neogene, the Pamir crust has been collapsing into the Tajik Depression, lateral material transport thickened the crust in the western Hindu Kush of Afghanistan in the Paleogene (Robert et al., 2017; Rutte et al., 2017).

Herein, we present Global Navigation Satellite System (GNSS) time series acquired between 2013 and 2016 along two densely spaced profiles—P1 and P2—ranging from the western Pamir Plateau across the northeastern Tajik-basin fold-thrust belt of the Peter the First Range into the southwestern Tian Shan (Figure 1b). We first review the regional tectonics (section 2), focusing on the regional seismicity, large earthquakes that were instrumentally observed in the region, geologic evidence of Quaternary fault-slip on the Vakhsh and the Darvaz fault zones, and recent rate estimates by geodetic measurements. In section 3, we introduce the new campaign GNSS data collected across the Vakhsh and Darvaz fault zones (Metzger et al., 2019). We detail the GNSS data collection, the data processing, and the rate estimation from the resulting time series. This includes measures for the effect of the 2015, M_w7.2 Sarez, Central Pamir, earthquake (Metzger et al., 2017; Sangha et al., 2017) on the rate estimates (section 4). We also assess the slip type and slip rate of the Darvaz and Vakhsh fault zones using kinematic modeling. In section 5, we integrate the geodetic, geologic, and seismic data and propose a conceptual model of the kinematic relationships between the western Pamir Plateau, the Tajik Depression, and the southwestern Tian Shan.

2. Neotectonic Setting

In the Pamir, northward displacement and crustal shortening is currently accommodated along the Vakhsh fault system and the Pamir thrust system in the north (e.g., Zubovich et al., 2010, 2016), the sinistral Darvaz fault zone in the west and northwest (Ischuk et al., 2013; Mohadjer et al., 2010), the dextral Aksu-Murghab (Ruzhentsev, 1963, 1968; Schurr et al., 2014; Strecker et al., 1995), and Karakorum (Chevalier et al., 2015; Sridevi et al., 2004) fault systems in the southeast, and the Kongur Shan-Tashkorgan normal fault system in the Chinese eastern Pamir (Chen et al., 2011; Liu, 1993), which also has a weak dextral component (Chevalier et al., 2015; Fan et al., 1994). Under the Pamir, Asian lithosphere forms a subduction arc that is retreating north and westward as traced by intermediate-depth (60–300 km) seismicity (Schneider et al., 2013; Sippl et al., 2013; Sippl et al., 2013). Kufner et al. (2016) suggested that Asian slab retreat is forced by indentation of the Indian lithosphere, bulldozing into the cratonic lithosphere of the Tajik-Tarim Basin at mantle depth.

In the Pamir interior, the active displacement field is composed of bulk northward movement combined with E-W extension (Ischuk et al., 2013; Zhou et al., 2016). The crust hosts both sinistral strike-slip faulting on NE striking or conjugate planes and—to a lesser degree—normal faulting on approximately north striking planes (Schurr et al., 2014). The only NE striking sinistral-transtensive fault system of the Pamir interior, which has a clear morphologic expression and is seismically active, is the Sarez-Karakul fault system that stretches from south of Lake Sarez to north of Lake Karakul (Figure 1b) (Rutte et al., 2017; Schurr et al., 2014; Strecker et al., 1995). The E-W extension is driven by westward gravitational collapse of thickened Pamir-Plateau crust into the Tajik Depression (Rutte et al., 2017;Schurr et al., 2014 ; Stübner et al., 2013), causing NW-SE shortening of the ~7–12 km thick sedimentary rocks of the Tajik Basin (Leith & Alvarez, 1985; Nikolaev, 2002). In the western Pamir Plateau, distributed strike-slip faulting accommodates shear between the northward moving Pamir and the Tajik Depression. The Darvaz fault splays off from the Pamir thrust system in a WSW direction and then curves south (Figures 1b and 1c). Farther southeast, the Badakhshan fault runs in parallel to the Darvaz fault. Offset morphologic features in central Badakhshan, Afghanistan, suggest dextral-transpressive slip (Schurr et al., 2014; Stübner et al., 2013), but neither geodetic nor seismic data constrain its kinematics.

2.1. Recent Crustal Seismicity

Crustal microseismicity (i.e., events with local magnitude smaller 4; hereafter called "seismicity") is focused along the perimeter of the Pamir, where it coincides with the Pamir thrust system in the north, the Peter the First Range in the northwest and the eastern Tajik Basin in the west (Figure 1b) (Kufner et al., 2018; Schurr et al., 2014). The interior of the Pamir also hosts seismicity following the Sarez-Karakul fault system (Schurr et al., 2014). The Badakhshan fault does not feature instrumentally recorded earthquakes.

In the Peter the First Range, seismicity is mostly located along the Darvaz fault and in between the Darvaz and the Vakhsh faults (Figure 1b) (Hamburger et al., 1992). Along the Darvaz fault seismicity clusters along its northern and southern segments. Three event catalogs, one combined from Schurr et al. (2014) and Kufner et al. (2018) with events recorded in 2008–2010 and in 2012–2014, respectively, one including events from the Soviet/US-CSE network operated during 1955–1979 (Hamburger et al., 1992), and events from teleseismic data recorded between 1970 and 2008 (Engdahl et al., 1998) all show the same seismically active features and areas of quiescence (Figure 2). In the Tajik Depression, seismicity is less prominent but distributed at the base and above the sedimentary cover at ~11 km. Sparse events occur in the basement down to 40 km depth, plus activity at the southern end of the Darvaz fault and where the Darvaz and the Vakhsh faults run in parallel, at ~71.5°E (Figure 1b).

Focal mechanisms available from the regional and global catalogs exhibit a nodal plane parallel to the curved outline of the Pamir (Figure 2) (Dziewonski et al., 1981; Ekström et al., 2012; Kufner et al., 2018; Schurr et al., 2014). The mechanisms along the Darvaz fault zone are mostly strike-slip but rotate to thrusting farther northeast. Earthquakes along the Ilyak fault zone have strike-slip mechanisms. Farther northeast, where the Ilyak transitions into the Vakhsh fault, thrusting becomes dominant and the epicenters are mostly located on the southeastern, downdip side of the fault. Even farther to the east, the global (M4.5+) CMT catalog (Storchak et al., 2013) contains a few strike-slip events that have similarities to the 1949, M_w7.6 Khait earthquake. A series of NW-SE aligned strike-slip events links the Darvaz and the

Vakhsh fault just close to our GNSS profile P1. The Tajik Depression west of the southern Darvaz fault hosts mostly thrust earthquakes with one subhorizontal nodal plane, likely indicating E-W oriented slip along a horizontal interface. There, features like the 800 m high Hoja Mumin diapir 20 km SW of Kulyab (Dooley et al., 2015) are attributed to salt tectonics (Figure 2).

Over the last 110 years, the Pamir region was struck by four M7+ crustal earthquakes: The 1949 Khait earthquake occurred at the northwestern perimeter of the Pamir, the 1974 Markansu earthquake at the northeastern perimeter and the 1911/2015 Sarez earthquakes in the Central Pamir (Figure 1b). The 1949, M_w7.6 Khait earthquake affected the area where the Darvaz and Vakhsh faults run in parallel (Figure 1b). This earthquake shows a NE-striking, sinistral and a NW striking dextral focal plane, probably rupturing a fault of ~60 km length (Kondorskaya & Shebalin, 1982; Kulikova, 2016; Storchak et al., 2013) either on the Vakhsh fault or in the southern Tian Shan (Schurr et al., 2014). We did not find reports on surface ruptures, but many landslides occurred (e.g., Evans et al., 2009), mostly in the area ~20 km northwest of the instrumentally derived epicenter (Figure 1b). The 1974, M_w7.1 Markansu earthquake activated the Pamir frontal thrust (Sippl et al., 2014).

The 1911, Ms~7.7 Lake Sarez earthquake was observed by a few analog, teleseismic stations and was located —with large uncertainties—~80 km west of the southern Sarez-Karakul fault system (Kulikova et al., 2015). Kulikova et al. (2015) and Schurr et al. (2014) argued that this earthquake ruptured the Sarez-Karakul fault system. The 2015, M_w7.2 Sarez, Central Pamir, earthquake has a strike-slip focal mechanism comparable to the 1911 Lake Sarez earthquake (USGS, 2015). Surface displacement maps from satellite imagery and neotectonic field mapping traced the rupture surface along the Sarez-Karakul fault system. The earthquake nucleated near Lake Sarez and propagated northeastward (Sangha et al., 2017). Metzger et al. (2017) observed coseismic slip of up to 3 m and modeled the source as a subvertical ~80 × 25 km fault plane comprising three segments. In addition, continuous GNSS stations in the eastern Alai valley (Figure 1b), ~120 km from the epicenter, and in northeastern Afghanistan, ~250 km from the epicenter, recorded horizontal offsets of a few millimeters up to 2 cm (see supporting information Figure S3 in Metzger et al., 2017). Stations on profile P1 are in a similar distance from the epicenter and thus might have been affected by the event as well (section 4.1).

2.2. Quaternary Deformation Rates

Quaternary faults in the western Pamir parallel the topographic margin of the Pamir Plateau (Burtman & Molnar, 1993; Trifonov, 1978). Neotectonic mapping located their activity primarily along the Darvaz fault zone. Offset geomorphologic markers—i.e., 20 m of late Holocene landforms, 120–150 m of early Holocene terraces and alluvial fans and 300 m of late Pleistocene landforms—suggest a sinistral slip rate of 10–15 mm/yr along the southern Darvaz fault at ~37.8°N (Trifonov, 1978). Farther north, at 38.5–38.7°N, the ~21 m displacement of a ~1,500 or 2,200 yr old, man-made defense structure suggests 10–40 mm/yr of sinistral slip (Kuchai & Trifonov, 1977). Offsets of Holocene (~160 m) and late Pleistocene (~800 m) valleys in the same area suggest 5–16 and 4–12 mm/yr, respectively (Nikonov, 1975, 1977; Trifonov, 1983).

Farther northeast, at ~39°N and ~71°20′E, Trifonov (1983) mapped 50–170 m sinistral and ~10 m vertical offsets of moraines, implying to 3–4 to ~8 mm/yr sinistral-transpressive slip rates since the last glacial maximum, assumed at ~20 ka (Burtman & Molnar, 1993). The mapped fault segments strike approximately E-W but an association with either the Vakhsh or the Darvaz fault is unclear. Where the Darvaz fault enters the Trans-Alai Range, at ~71.4°E, it seems to become inactive.

Neotectonic deformation along the Vakhsh fault comprises a 9–12 km wide belt of thrust and reverse faults along the northern slope of Peter the First Range (Burtman & Molnar, 1993). Trifonov (1983) reported 10–15 m of dextral offsets of dry valleys at 70.5°E, east of Garm. Furthermore, ^{14}C ages of 670 ± 40, 1470 ± 100, and 2000 ± 100 yr from swamp deposits dammed by tectonic scarps suggest recent tectonic activity.

The Tajik Basin shortens NW-SE, indicated by Quaternary, right-lateral displacements along the major faults at its northern rim (Zakharov, 1948, 1955, 1958). Dextral displacements of Holocene landforms (~15 m) occurred along approximately east striking faults (Legler & Przhiyalgovskaya, 1979), and of late Pleistocene terraces (~90 m) along approximately NE striking faults (Trifonov, 1983). These faults are likely part of the Ilyak fault system and the faults of the Tajik-basin fold-thrust belt that are dragged right-laterally

into the Ilyak fault zone. Within the fold-thrust belt, sinistral offsets of late Pleistocene and Holocene landforms occurred along N-NE striking, oblique-reverse faults (Nikonov, 1970; Trifonov, 1983).

2.3. Geodetic Deformation Rates

The estimated geodetic slip rate for the Darvaz fault from a sparse regional geodetic array is 10 ± 1 mm/yr (Ischuk et al., 2013). Given the interstation distance of 250 km, it is unclear whether this deformation is accommodated by the Darvaz fault or within the Tajik-basin fold-thrust belt. Zhou et al. (2016) estimated ~7 mm/yr of N-S shortening either on the Vakhsh fault, the Darvaz fault, or on any structure in-between. Farther north, where the Darvaz fault approaches the Vakhsh fault and links with the Pamir thrust system, continuous GNSS stations indicate a minimum of 5.6 ± 0.8 mm/yr dextral shear and 2.2 ± 0.8 mm/yr N-S shortening on one of the fault strands of the Pamir thrust system (Zubovich et al., 2016).

Slip on the Vakhsh fault near the Garm region, the northwestern Peter the First Range (Figure 1b) was observed using leveling and laser-ranging techniques since 1948/1950 and 1968, respectively. A 317° trending, 6 km long triangulation and leveling network revealed a relative rate of 16 ± 1 mm/yr between the Peter the First Range and the southern Tian Shan (Guseva, 1986; Konolpatsev, 1971). Given the fault strike, this corresponds to ~6 mm/yr of dextral shear along and ~15 mm/yr of shortening across the Vakhsh fault, but this may only capture a portion of the full strain accumulation across the fault and could point to (postseismic) fault creep. The rates were confirmed by an independent network measured in 1972 and 1980, spanning less than 1 km across the fault scarp: The relative horizontal rate was 15.9 ± 0.5 mm/yr with respect to the markers in the southern Tian Shan (Guseva, 1986). A remeasurement of the original profile using laser-ranging devices in 1974–1984 resulted in a more complicated pattern, with ~8 mm/yr of convergence across the Vakhsh fault, and ~4 mm/yr of shortening within the northernmost 4 km of Peter the First Range. If the pattern changes are significant, they might reflect the return from the postseismic (afterslip or creeping) stage after the 1949, M_w7.6 Khait earthquake to the (locked) interseismic stage.

The leveling data acquired over 5 to 29 years showed no uplift on the northwestern side of the Vakhsh river in the southwestern Tian Shan, but 7–9 mm/yr of relative uplift on its southeastern side that rapidly decreased to 1–4 mm/yr southeastward (Guseva, 1986), suggesting a listric geometry for the Vakhsh fault with a rapidly decreasing southeast dip (Burtman & Molnar, 1993). Another 1 km profile across the Vakhsh thrust revealed even higher uplift rates, 18.6–21.6 mm/yr. A 200 m long dense leveling profile in a tunnel dug across the Vakhsh thrust yielded a relative uplift rate of 14.6 ± 0.3 mm/yr between 1973 and 1976, pointing to a steeply S dipping fault. Using borehole data across the Vakhsh thrust, Guseva (1986) determined a 48° dip.

3. GNSS Data Collection, Processing, and Rate Estimation

3.1. Marker Installation and Instrument Setup

In 2013, we installed 21 GNSS markers in the northwestern Pamir with a focus on the Vakhsh and the Darvaz faults (Figure 1b). We placed the network such that it forms two profiles (P1 and P2), crossing these faults subperpendicularly. The network also included four stations of the survey of Ischuk et al. (2013), where we prolonged the time series. Profile P1 crosses the Peter the First Range and includes 14 points. It has a length of ~230 km and extends from ~50 km NW of Garm to ~40 km SE of the Panj-Bartang river junction (Figure 2). Profile P2 is located ~100 km farther southwest and covers the Pamir foothills and the northeastern Tajik Basin from the Panj river to 50 km ESE of Dushanbe with a total length of ~200 km. It contains seven new data points, of which one was destroyed in 2014. The profile has a kink to better image fault-parallel and fault-perpendicular rates (section 4.2). Average interstation distances are 10 km and 15 km for P1 and P2, respectively.

The GNSS markers are 10 cm long stainless steel bolts of 1 cm diameter that were drilled and glued into the bedrock. The minimalistic design contains only a small dimple to fix the tip of the tripod (Figure S1a in the supporting information).

We used three Trimble Zephyr Geodetic Model 1 antennas (TRM 41249.00) and three Trimble R7 receivers to acquire the data. The antennas were installed on top of portable, short-braced aluminum tripods (Figure S1b), locked to the ground with rocks to stabilize the set up (Figures S1b and S1c). The antenna was aligned to true North. We recorded data for 40–48 hr per campaign (i.e., two consecutive nights) with a

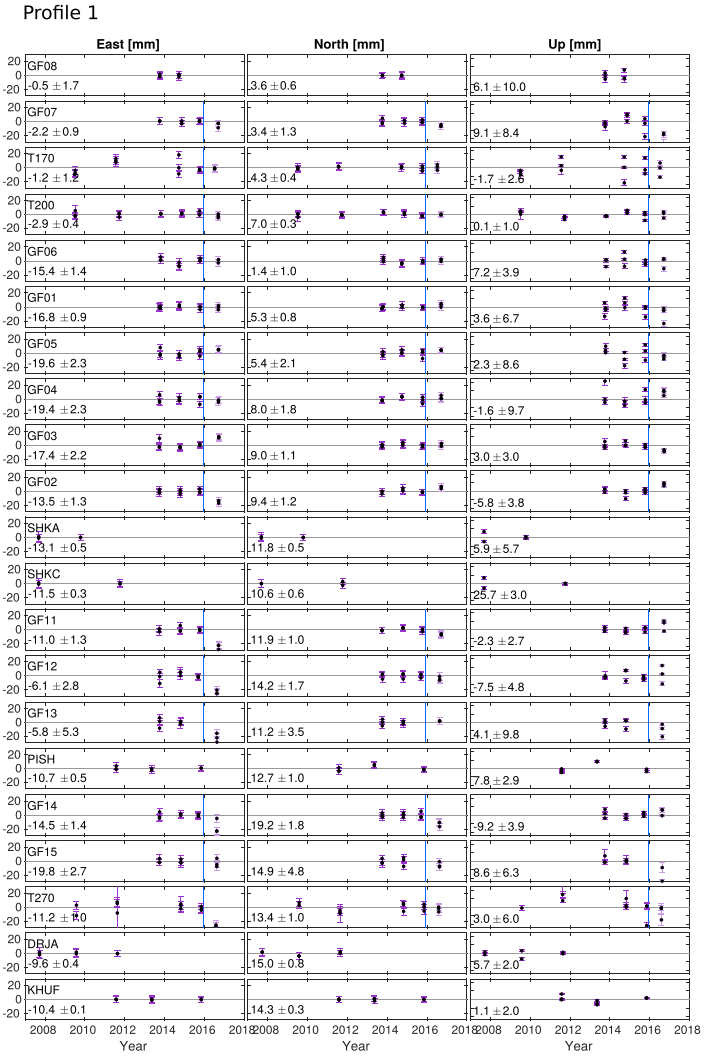

Figure 3. East (left column), north (center), and vertical (right) GNSS time series residuals after removing a linear velocity fitting the data until 2015. The stations are sorted along Profiles P1 (here) and P2 (continued figure). The vertical blue line marks the M_w7.2 Sarez earthquake. Rates obtained from data acquired before the earthquake are indicated in each subfigure.

sampling rate of 30 s. To minimize seasonal loading signals, we collected the data in fall (September to November) of the years 2013 to 2016. The slope steepness near the measurement sites in the northwestern Pamir reaches 45° leading to limited space aperture (Figures S1c and S1d).

3.2. Data Processing

The raw data were converted into daily, receiver-independent exchange format (RNX) files, which were published in Metzger et al. (2019). They were processed together with 24 reference stations of the International Global Navigation Satellite System Service (IGS) network and RNX data of Ischuk et al. (2013) and Zhou et al. (2016), using the Earth Parameter and Orbit System software (Deng et al., 2016). The processing includes ionosphere-free linear combination, undifference carrier phase and pseudo-range observables, IGS08 absolute phase center variations (Schmid et al., 2016) and the FES2004 ocean tide loading model (Lyard et al., 2006). Apriori zenith hydrostatic delay is obtained using the Global Pressure and Temperature model (GPT2) and the Vienna mapping function in a grid file database. Station coordinates and tropospheric wet zenith delays are estimated using random-walk parameters for every two hours

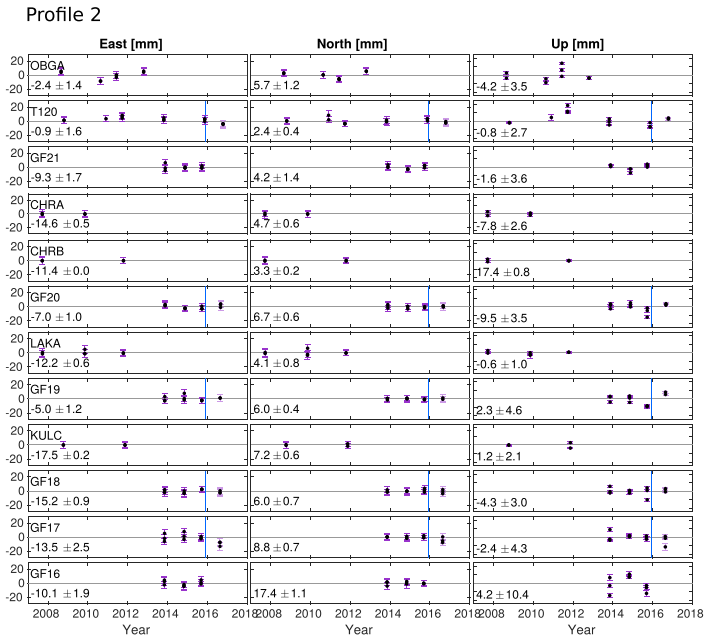

Figure 3. (continued)

(Gendt et al., 2013). In order to ensure consistency in the processing, we applied reprocessed GNSS precise satellite orbits as well as clock products obtained by the Earth Parameter and Orbit System software using the same parameter setup as for the station coordinate estimation (Gendt et al., 2013). Additionally, station coordinates were estimated in network mode and aligned to the IGS 2nd combined daily coordinate product (ITRF14), reducing the impact of the Earth rotation parameter (Altamimi et al., 2016; Rebischung et al., 2016). As a quality measure, daily observation files with continued observations shorter than 1 hr were excluded. With very few exceptions, the data quality is very good and the positions are consistent. The standard deviation of the daily positions per measurement is 2.1 mm (Figure 3). In the vertical direction, the standard deviation is 4 times larger (8.1 mm).

3.3. Rate Estimates

From the daily positions, we built time series and estimated the interseismic deformation rates individually for each station and component. By a visual inspection, we excluded outliers and then applied a two-parameter, linear rate estimation using a least squares inversion (Figure 3). All data points were weighted with their instrumental error. Following (Geirsson et al., 2006), we normalized the estimated rate uncertainty σ by the total observation period ΔT between the first and the last measurement of the time series, with N being the total number of positioning data points, and the daily position y_i being predicted by model point $\hat{y}_i$,

$$\sigma = \frac{\sum_{i=1}^{N}(y_i - \hat{y}_i)^2}{\sqrt{N-2}} \cdot \frac{1}{\Delta T}.$$

This means that for time series with a short observation period of 2 or 3 years the rate uncertainty can be rather large. The average misfit of the rate estimation is 0.8 mm/yr in North, 0.5 mm/yr in East and 2.0 mm/yr in the vertical component, which is good, given the steep topography and limited space aperture. The derived rates and uncertainties are provided both in the ITRF14 no-net-rotation (NNR) reference frame (Altamimi et al., 2016) and in a Eurasian-fixed reference frame (Table 1) (Altamimi et al., 2017) in the supporting information ("GNSSratesITRF14_NNR.txt," "GNSSratesITRF14_EU.txt"). The data show no apparent bias in the residuals apart from a distinct offset between data collected until the 2015 campaign and after (Figure 3), which will be discussed in section 4.1.

Table 1
Eurasian-Stable Rates v and 1σ Uncertainties (Altamimi et al., 2017) for East, North, and Vertical Components, Obtained From a Combined Network Solution of New and Updated Data (Ischuk et al., 2013; Zhou et al., 2016; Zubovich et al., 2010)

			Rates 2013–2015 (mm/yr)						Rates 2013–2016 (mm/yr)						
Name	Lon. (°)	Lat. (°)	*vE*	*vN*	*vU*	*σE*	*σN*	*σU*	*vE*	*vN*	*vU*	*σE*	*σN*	*σU*	Δ*T* (yr)
GF01	70.2383	38.7988	−16.8	5.4	3.6	0.9	0.8	6.7	−17.0	6.1	0.2	0.7	0.7	5.0	3/2
GF02	70.7105	38.6884	−13.5	9.4	−5.8	1.3	1.2	3.8	−17.6	11.0	−0.9	1.7	0.9	3.0	3/2
GF03	70.6252	38.7486	−17.4	9.0	3.0	2.2	1.1	3.0	−14.0	9.2	−0.6	1.8	0.7	2.1	3/2
GF04	70.3533	38.7334	−19.4	8.1	−1.6	2.3	1.8	9.7	−20.1	8.8	3.1	1.3	1.2	6.0	3/2
GF05	70.3262	38.7770	−19.6	5.4	2.3	2.3	2.1	8.6	−18.1	6.7	−0.3	1.4	1.3	4.9	3/2
GF06	70.1889	38.8340	−15.4	1.4	7.2	1.4	1.0	3.9	−15.4	1.4	7.2	1.4	1.0	3.9	3/3
GF07	69.9355	38.9064	−2.2	3.4	9.1	0.9	1.4	8.4	−3.5	1.6	−0.4	0.9	1.0	6.1	3/2
GF08	70.1893	39.1908	−0.5	3.6	6.1	1.7	0.6	10.0	−0.5	3.6	6.1	1.7	0.6	10.0	1/1
GF11	70.7643	38.5774	−11.0	11.9	−2.3	1.3	1.0	2.7	−17.9	10.0	1.3	2.7	0.9	2.7	3/2
GF12	70.8109	38.4467	−6.1	14.2	−7.5	2.8	1.7	4.8	−12.8	13.0	−5.6	3.1	1.2	4.4	3/2
GF13	71.0280	38.4664	−5.8	11.2	4.1	5.3	3.5	9.8	−13.9	12.0	−1.7	2.4	1.0	4.1	3/1
GF14	71.2691	38.3146	−14.5	19.2	−9.2	1.5	1.8	3.9	−19.5	15.6	−6.9	2.5	1.7	2.7	3/2
GF15	71.3850	38.1908	−19.8	14.9	8.6	2.7	4.8	6.3	−20.8	13.0	−6.7	1.4	1.6	4.6	3/1
GF16	70.4449	38.1034	−10.1	17.4	4.2	1.9	1.1	10.5	−10.1	17.4	4.2	1.9	1.1	10.5	2
GF17	70.1721	37.9496	−13.5	8.9	−2.4	2.5	0.7	4.3	−16.4	7.6	−4.0	1.8	0.9	3.3	3/2
GF18	69.8604	38.0061	−15.2	6.0	−4.3	0.9	0.8	3.0	−15.2	6.0	−4.3	0.9	0.8	3.0	3
GF19	69.5762	37.9839	−5.0	6.0	2.3	1.2	0.4	4.6	−5.0	6.0	2.3	1.2	0.4	4.6	3
GF20	69.2454	38.3459	−7.0	6.7	−9.5	1.0	0.6	3.5	−7.0	6.7	−9.5	1.0	0.6	3.5	3
GF21	69.1845	38.4673	−9.3	4.2	−1.6	1.7	1.4	3.6	−9.3	4.2	−1.6	1.7	1.4	3.6	2
T120[a]	69.4213	38.5852	−0.9	2.4	−0.8	1.6	0.4	2.7	−0.9	2.4	−0.8	1.6	0.4	2.7	8
T170[a]	70.2012	39.1204	−1.2	4.3	−1.7	1.2	0.4	2.6	−1.2	4.3	−1.7	1.2	0.4	2.6	7
T200[a]	70.0563	38.8691	−2.9	7.0	0.1	0.4	0.3	1.0	−2.9	7.0	0.1	0.4	0.3	1.0	7
T270[a]	71.6630	38.0032	−11.2	13.4	3.0	1.0	1.0	6.0	−13.7	13.2	2.4	1.7	0.8	4.8	7/6

Note. Δ*T* indicates time series length, if the 2016 data acquisitions are excluded or included, respectively. The full network solution (with additional rates of 51 locations) is available in the supporting information (GNSSratesITRF14_EU.txt and GNSSratesITRF14_NNR.txt).
[a]Extended time series of Ischuk et al. (2013).

The obtained rates were then compared to an independent processing run using the GAMIT/GLOBK software package (Herring et al., 2018a, 2018b). In this run, we combined positions of 25 regional continuous and IGS stations with 66 campaign stations throughout the region using GAMIT to calculate initial daily positions, which were then edited, averaged, and weighted over ~2 week long intervals. Then, GLOBK's Kalman filter (Herring et al., 2015) was used to estimate linear horizontal velocities from the position averages within the ITRF08 reference frame (Altamimi et al., 2012), incorporating a random walk noise model to account for systematic errors. The mean difference between the two data sets is 1.7 ± 2.3 mm/yr in the east direction and −0.3 ± 1.2 mm/yr in the north direction.

4. Results and Interpretation

4.1. Potential Influence of the 2015, M_w7.2 Sarez Earthquake on the Time Series

Some GNSS positions of the 2016 campaign show a clear offset from the (assumed) linear rate trend provided by the measurements acquired prior to 2016 (in Figure 3 and Table S1). This is most prominent at stations T270, GF11, GF12, GF13, GF14, and GF02, with 5–20 mm offsets toward the west. Station GF03 exhibits an 11 mm offset toward the east. Together, these stations suggest dextral motion on the Darvaz fault, which is opposite the sense of interseismic loading. This signal is not a measurement bias, for example, from seasonal variations, which are to be expected to be in the order of a few millimeters (Dong et al., 2002) or neglected firmware updates. We also rule out artifacts caused by instrument types or setup (Table S1). Therefore, we interpret the signal to reflect real ground displacements. Stations with large offsets between the 2015 and 2016 campaigns are located near the Darvaz fault, with amplitudes generally decreasing from SE to NW and an abrupt sign change across the Darvaz fault (Figure 4 and Table S1). Station GF15 is an exception but was not measured in 2015. The displacement pattern resembles either a dextral slip event or transient creep on the Darvaz fault with fault slip of centimeters to decimeters.

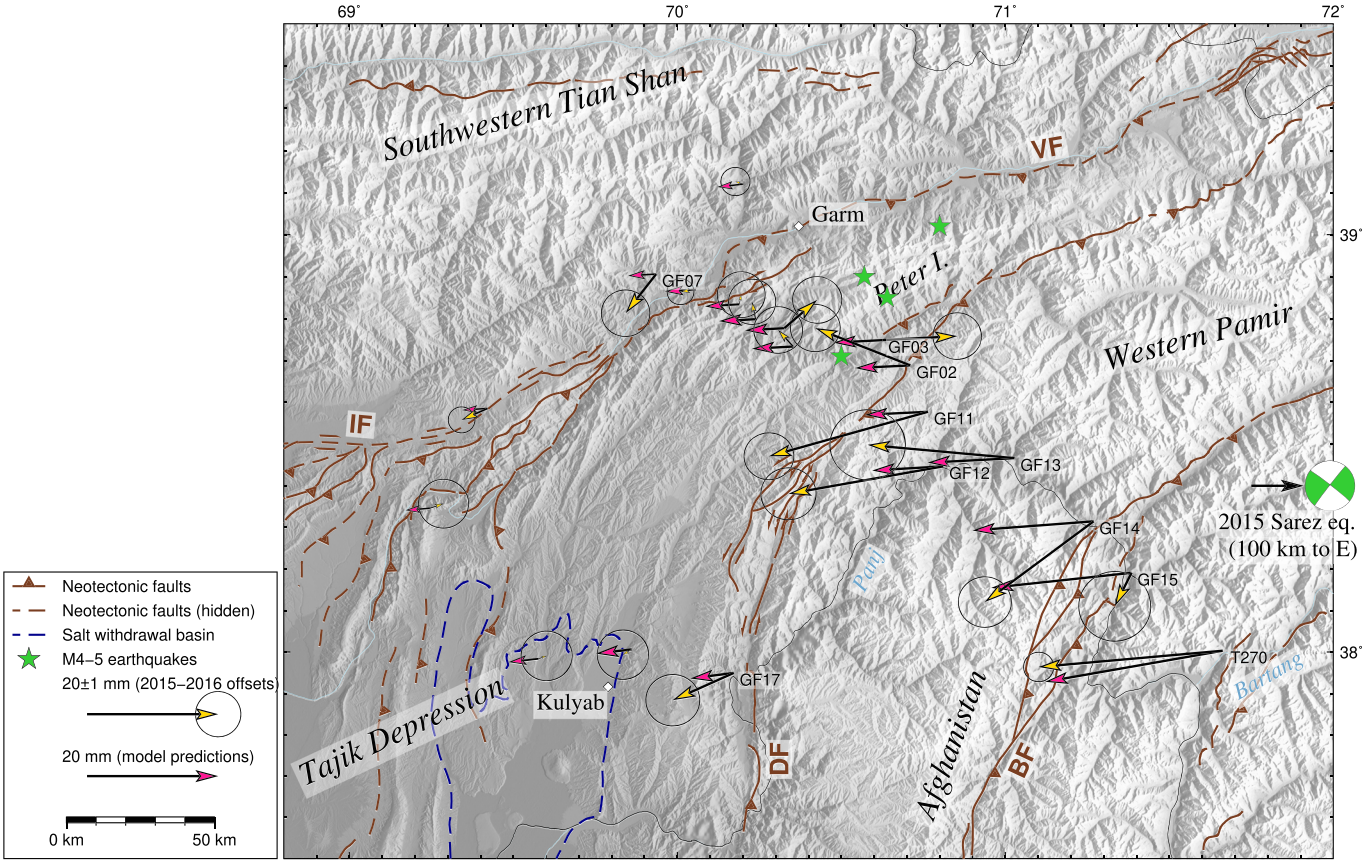

Figure 4. GNSS positioning differences between the 2015 and 2016 data surveys (yellow arrows, 2σ confidence level) in comparison to the coseismic displacements (pink arrows) of the M_w 7.2 Sarez earthquake (green focal mechanism) as predicted using the slip model of Metzger et al. (2017). Green stars mark the M4–5 earthquakes that occurred between the 2015 and 2016 surveys (see also Tables S1 and S2 in the supporting information).

Several instrumentally recorded earthquakes occurred between the two measurement periods in fall 2015 and 2016. To understand their effect on our time series, we investigated if these events could have caused a coseismic displacement of the order of a few centimeters on the mentioned stations. We consider both, the 7 December 2015, M_w7.2 Sarez earthquake discussed above (Metzger et al., 2017; Sangha et al., 2017) and a series of crustal M4–5 earthquakes near the Darvaz fault (Figure 4 and Table S2) (GEOFON Data Centre, 1993). For the largest event of this series, the M5.1, 1 July 2016 earthquake, we checked, if satellite radar interferometry (Sentinel-1, acquired on 27 May and 14 July 2016) shows a signal comparable to the GNSS-derived offsets, but did not find one. We forward modeled a series of slip events with random source-parameter combinations following scaling laws (Mai & Beroza, 2000) to see if they cause a displacement pattern similar to the observed GNSS offsets. We used rectangular dislocations in an elastic half-space (Okada, 1985) and refer to section 4.3 for more modeling details. None of the synthetic models predict more than 1 cm offset, unless the source is located only a few hundred meters deep. But according to these models, a shallow source would not have affected stations at distance of 100 km, like station GF14 and T270. We therefore suggest that the offset signal was caused by the M_w7.2 Sarez earthquake. This hypothesis is also supported by satellite radar interferometry (Metzger et al., 2018) and 1 Hz-GNSS data acquired across the Pamir thrust system in the Alai valley (Zubovich et al., 2016) (Figure 1b): The coseismic interferograms show a distinct surface rupture of a strand of the Pamir thrust system of a few millimeters to centimeters. The 1 Hz-GNSS stations recorded coseismic static displacement of a couple of centimeters, with a slip-sense opposite to the expected loading direction, in a similar distance to the earthquake epicenter as the stations presented here (Metzger et al., 2018). Using the distributed slip model of Metzger et al. (2017), we predict the expected displacement in the region of the Darvaz fault (Figure 4). The results match the amplitudes, but do not explain the rapid signal decay across the Darvaz fault or the eastward offset of station GF03. Instead the offset azimuth remains constant and the amplitudes decay quasi-linear with increasing distance to the Sarez

rupture. The GNSS observations on the sinistral-transpressive Darvaz fault and the dextral-transpressive Pamir thrust system show a pattern which is opposite to the interseismic loading sense, suggesting fault loading, probably triggered by the Sarez earthquake. We thus decided to exclude the data acquired in 2016 from the analysis of the interseismic deformation rates below.

4.2. Interseismic Rates 2013–2015

Based on the acquisitions between 2013 and 2015 we present horizontal and vertical interseismic GNSS rates relative to stable Eurasia (Altamimi et al., 2017) in map view (Figure 5). We also decompose the rates along profiles P1 and P2, into profile-perpendicular and profile -parallel components, where the former roughly represent shortening/extension and the latter shear across the Darvaz and or Vakhsh or Ilyak faults (Figure 6). In doing so, we projected all GNSS points and seismologic data in a 120 km wide profile swath onto the profiles.

The western Pamir-Plateau stations move at ~17 mm/yr toward northwest relative to Eurasia (Figure 5a). When crossing the Darvaz fault the rates of the profile P1 stations decrease slightly and the displacement vectors rotate from NW toward WNW (GF04, GF01, GF05, and GF06). Across the Vakhsh fault, the rates drop to 5 mm/yr N (T200, GF07, T170, and GF08). Along profile P2, the stations exhibit an increasingly more westerly orientated motion when crossing the Darvaz fault from east to west (GF16, GF17, GF18, and KULC). This westerly displacement vanishes across the Ilyak fault (T120 and OBGA). The slow rate at GF19 stands out from the adjacent stations GF18, KULK, and LAKA. This station—located within the salt withdrawal basin near Kulyab—might be influenced by the active salt tectonics. Overall, the strongest internal deformation is observed in the Tajik-basin fold-thrust belt and along its northern margin, whereas the western Pamir-Plateau and the southwestern Tian Shan exhibit minor internal deformation.

Vertical velocities obtained from stations with more than two measurement campaigns (Figure 5b) are less significant but suggest that the southwestern Tian Shan north of Dushanbe is subsiding 5–10 mm (e.g., station OBGA) while the southwestern Tian Shan farther east appears stable (T170 and T200). In the Peter the First Range, uplift is gradually increasing toward the Vakhsh fault (GF05, GF01, and GF06). In the western Pamir Plateau, the values are more heterogeneous and vary between ±10 mm/yr. Stations in the Tajik Depression show mostly subsidence.

Along profile P1, the most significant feature of the profile-perpendicular and profile-parallel rate (Figures 6c and 6e) is the rate change across the Vakhsh fault, which amounts to ≥17 mm/yr in the profile-parallel direction (shortening) and ≥ 13 mm/yr in the profile-perpendicular direction (consistent dextral slip sense). The profile-perpendicular rate gradient is steeper than in profile-parallel direction and could be classified as an offset. In classic screw dislocation models the steepness of the rate change across a fault is inverse proportional to the locking depth (Segall, 2010); thus, a step function suggests that a fault is freely creeping. Consequently, shear and shortening might be partitioned in the upper part of the Vakhsh, with its most shallow section dominated by strike-slip and the deeper part by shortening. Along the Darvaz fault, the data suggest a locked fault that accommodates ~10 mm/yr of profile-parallel extension and ~15 mm/yr of sinistral (profile-perpendicular) shear (Figures 6c and 6e). The Badakhshan fault may accommodate 5–10 mm/yr dextral shear, but the uncertainties are large and the station spacing is large.

The geodetic data are in agreement with the focal mechanisms of Kufner et al. (2018) that suggest thrusting with a dextral component along the Vakhsh fault and predominantly sinistral shear along the Darvaz fault (Figures 2 and 6a). The abundant seismicity underneath Peter the First Range reaches in excess 20 km. Below 5–10 km it probably outlines steeply NW dipping faults in the crystalline basement rocks underneath the Tajik-basin deposits (Kufner et al., 2018). Along the southeastern margin of the Peter the First Range the seismicity delineates a near-vertical structure along the Darvaz fault; it then significantly decreases toward SE (Figure 6a). Local, vertically aligned seismicity occurs near the Badakhshan fault, but in map view, it is apparent that this seismicity is associated with a small cluster and not outlining a major fault zone (Figure 2).

In general, the rate changes along profile P2 are harder to interpret than along profile P1, as the station distances are larger. Both the Ilyak fault and the Darvaz fault seem to be less active than along profile P1 (Figures 6d and 6f). The Ilyak fault accommodates ~5 mm/yr of shortening and 8–15 mm/yr of dextral slip, which is in agreement with the dextral focal mechanisms (Figure 6b) associated with earthquakes occurring

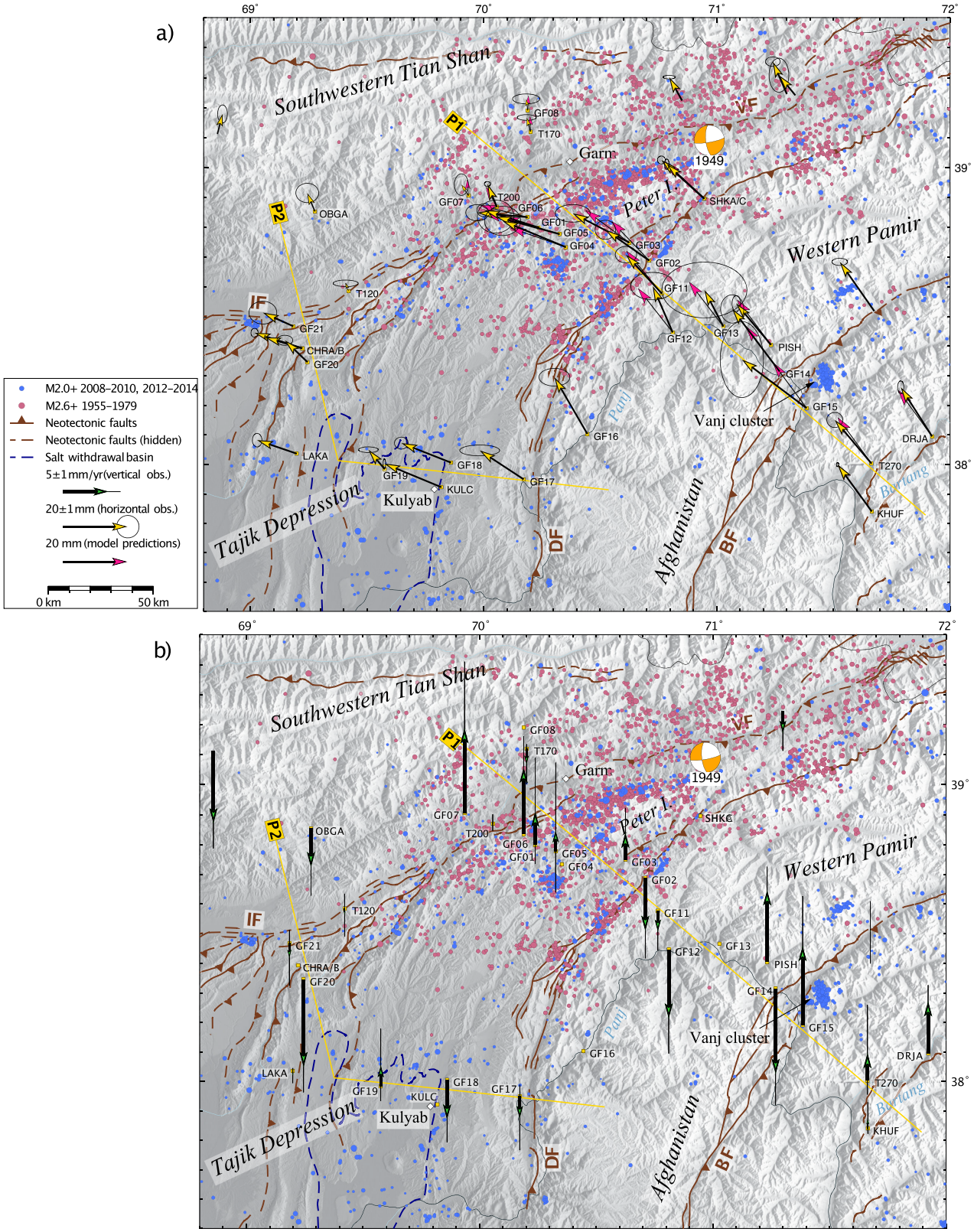

Figure 5. Horizontal and (b) vertical GNSS rates measured between 2013 and 2015 with 2σ uncertainties in a Eurasian reference frame (Altamimi et al., 2017). Pink arrows in (a) are the modeled rates (see section 4.3). Note the different rate scale in (a) and (b). Yellow lines mark Profiles P1 and P2, crustal seismicity of Hamburger et al. (1992) in red, and Kufner et al. (2018) in blue.

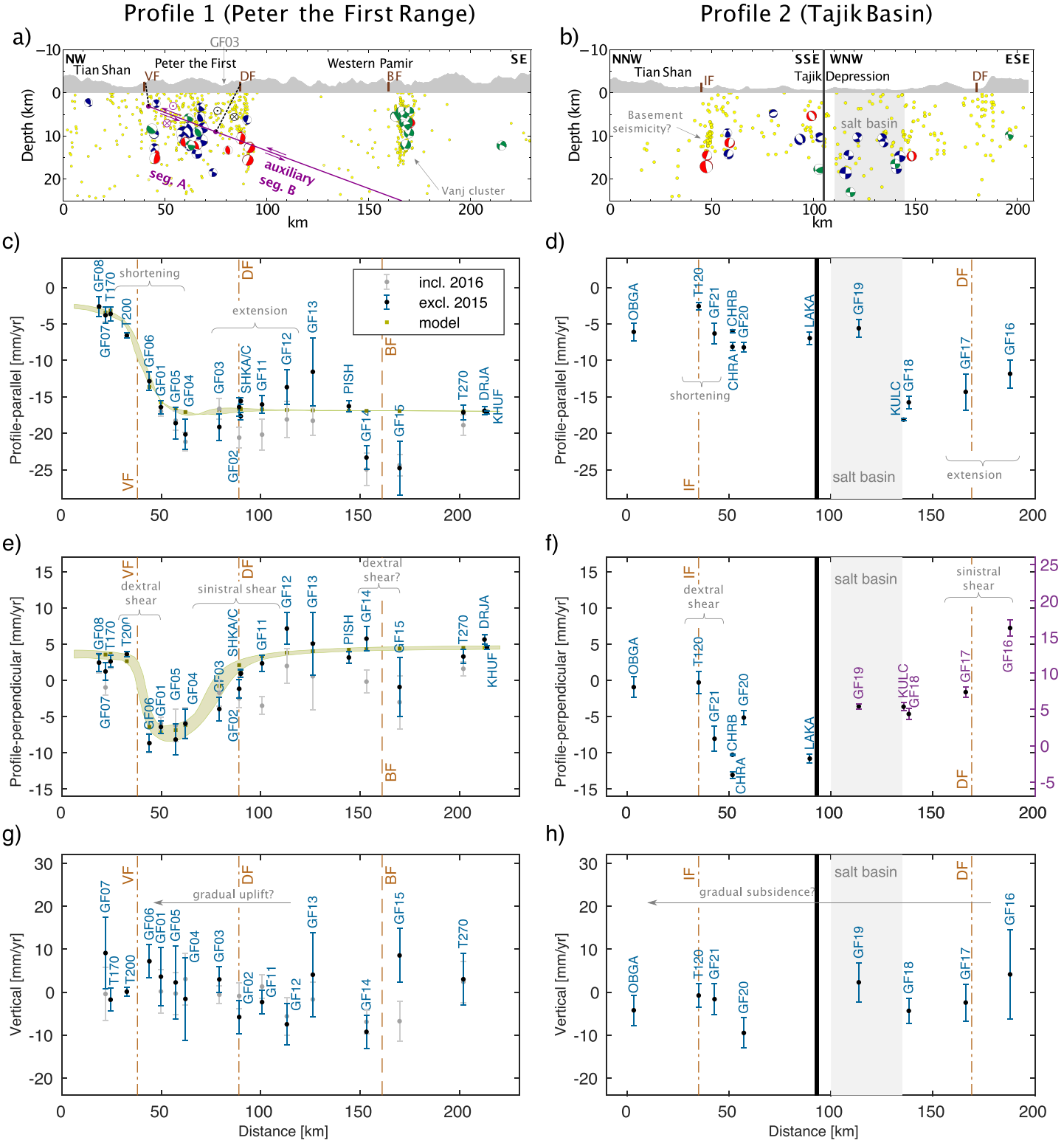

Figure 6. (a) and (b) Topography (enhanced by factor 10) and seismicity of a 120 km wide swath (Kufner et al., 2018) along Profiles P1 and P2, respectively. Violet lines mark model Segment A and auxiliary Segment B including slip sense, dashed lines symbolize the locking depths of the Vakhsh fault and the Darvaz fault (section 4.3). Note in (b) that the Vanj cluster is not along the Badakhshan fault (BF). IF = Ilyak fault; VF = Vakhsh fault. The GNSS velocities with 1σ uncertainties along Profile P1 (c, e, and g) and Profile 2 (d, f, and h) are resolved in profile-parallel (c and d), profile-perpendicular (e and f), and vertical components (g and h). The gray velocities include the 2016 campaign data; the blue rates exclude them. In (c) and (e) the slip model predictions are plotted for each GNSS data point (olive green squares) and—within 2σ uncertainties—for profile P1 (olive green band).

in the basement rocks below the Tajik-basin strata (Kufner et al., 2018). The rate change between station GF16 and GF17, at ~20 km profile-perpendicular distance across the Darvaz fault zone, suggests 8 ± 1 mm/yr sinistral shear and 2 ± 2 mm/yr extension along the Darvaz fault zone. Also along profile P2, the Darvaz fault is outlined by focused seismicity: The only constrained focal mechanism is in agreement with its sinistral kinematics (Figure 6b).

The vertical rates along profile P1 imply a gradual increasing uplift of a few millimeters of the stations NW of the Darvaz and a gradual subsidence of 5–7 mm/yr on the SE side of the fault (Figure 6g). The stations SE of the Badakhshan fault show uplift of 0–10 mm/yr. The stations along profile P2 indicate a gradual change from uplift of 0–5 mm/yr in the western Pamir Plateau to subsidence of 0–10 mm/yr in the Tajik Depression (Figure 6h).

4.3. Kinematic Modeling

To numerically assess the kinematic parameters of the Darvaz and the Vakhsh faults, we simulated fault slip using rectangular dislocations in an elastic half-space (Okada, 1985) with a rigidity of 30 GPa. The complex geologic structure of the Peter the First Range would be best represented with a three-dimensional model. However, since the GNSS data are aligned along profiles P1 and P2, with the highest station density along profile P1, a three-dimensional model would rely on strongly constrained geometric model parameters. Consequently, we simplified the geometry to two dimensions by focusing on the rates observed along profile P1, which is sub-perpendicular to the Darvaz and the Vakhsh faults. We neglected the curved fault geometry while assuming infinite fault length and downdip extent. We tested fault geometries with up to five segments, also to come up with the potential slip partitioning in the upper part of the Vakhsh fault (section 4.2; Figures 6c and 6e), but the amount of data was too sparse to stabilize the results. The best data fit—using the smallest number of free model parameters—was obtained with a 10° SE dipping plane representing the Vakhsh thrust, following the basal décollement in the Jurassic evaporites. This geometry corresponds on first order to the geologic cross sections of Chapman et al. (2017) and Hamburger et al. (1992) and the seismicity (Kufner et al., 2018) (Figure 6a). Our modeling setup implies that the Darvaz fault is locked until it merges with the basal décollement. Free parameters are the fault strike and location, the locking depth, that is, the depth of the upper edge of the dipping plane (Figure 6a). We further solved for dip-slip, along-strike slip and fault strike on two subsegments—Segments A and B—with the downdip extent of Segment A as another free parameter (Figure 6a). Including two parameters for a reference frame correction we solve for ten free parameters. The best fit model parameters were first constrained by a Monte Carlo type, simulated annealing approach (Cervelli et al., 2001) that over time gradually favors parameter combinations producing low misfits. This approach minimizes the chance to get trapped in a local minimum of the multidimensional parameter space. Then, we used the outcome of the annealing as a starting point for a classical nonlinear least squares inversion. The model parameter uncertainties were assessed in 500 additional runs using bootstrapping, in which the input of one GNSS station is randomly replaced by another (Efron, 1979).

The preferred model has a fault strike of 049° + 6°/−8°, which is similar to the average strike of the Darvaz and the Vakhsh faults along profile P1. Slip only occurs below 3.1 + 0.5/−0.8 km, meaning that the upper part of the Vakhsh fault is locked (outlined by the dashed line in Figure 6a). Under the Peter the First Range, Segment A accommodates 16 ±3 mm/yr of profile-parallel dextral shear and 15 + 4/−2 mm/yr of profile-perpendicular shortening. Segment B begins near station GF03 (Figure 6a) and shear flips to a sinistral 1 + 2/−3 mm/yr rate but with a constant 16 + 1/−1 mm/yr shortening rate. Segment B represents the northwestward (block) motion of the western Pamir-Plateau crust; its geometry is quite arbitrary, except that the intersection between Segments A and B places the connection between the Darvaz fault and the basal décollement of the Vakhsh thrust at 9.0 + 0.4/−0.8 km (dashed lines in Figure 6a). Thus, the difference in shear between Segments A and B is interpreted to be accommodated by the Darvaz fault; the along-strike slip difference is 15 + 4/−5 mm/yr. Apart from a few stations near the Badakhshan fault, which we do not include in our model and which also exhibits large rate uncertainties, the fit between the observations and the model is good (Figure 5a). In the Peter the First Range, the shear and shortening rates are systematically underrepresented by a few millimeters (olive green squares in Figure 5a). The model slightly underestimates the profile-parallel rates of GF03-05

and is unable to reproduce the abrupt rate decrease, in particular the profile-perpendicular rates between T200 and GF06 across the Vakhsh fault. This shows that near the surface, the locking regime must be more complex than our preferred model can predict; this is in accordance with our inference (section 4.2) of slip partitioning and possible creep in the shallow section of the Vakhsh fault.

The parameter uncertainty analysis reveals strong correlation among several parameters, manifested by elongated and curved scatter plots of best fit parameters obtained from bootstrapping (Figure S2): A deeper locking depth of the Vakhsh fault calls for a shorter width of Segment A, higher dextral shear rates on Segment A and (in opposite sense) Segment B, and a more easterly fault strike. Even within the 2σ uncertainties (95% confidence), the model fails to fit the profile-parallel rate of GF04 and the profile-perpendicular rate of GF06 (olive green band in Figures 6c and 6e).

5. Discussion

Given the low temporal resolution of survey mode GNSS data, we cannot uniquely link the offsets observed on GNSS stations between the 2015 and the 2016 campaigns to the 2015 M_w7.2 Sarez earthquake or other nearby earthquakes (see section 4.1). If we include the 2016 data for the estimation of the GNSS rates, the observed fault slip rates on the Darvaz drop to a few mm of shortening and $\leq$9 mm/yr of sinistral slip (gray data in Figure 6a), which is less than what the neotectonic slip rates suggest. If true, the estimated slip rates presented in section 4.2 would reflect an upper bound only and/or the Darvaz fault would be less active than presumed. We also tried to correct the 2016 positions using the surface displacement predicted by the coseismic slip model of the 2015 Sarez earthquake of that exhibits sinistral slip of up to 3 m on a subvertical, NE striking, 80 km long fault (Figure S3) (Metzger et al., 2017). This increases the slip rates only slightly and the quasi-linear decay of the predicted displacements from ENE to WSW (Figure 4) does not explain the observed offsets satisfyingly. Therefore, we suggest that the Darvaz fault was activated during the 2015 Sarez earthquake and produced dextral coseismic slip of a few centimeters, opposite to its interseismic slip.

Triggered slip phenomena are not yet well studied, as the focus of the scientific community lies on the activity of the main event. But due to an increased spatial resolution, e. g. using Synthetic Aperture Radar interferometry (Price & Sandwell, 1998; Wei et al., 2011; Wright et al., 2001) or high instrumental sensitivity, for example, using creep meters (Bodin et al., 1994; Victor et al., 2018), we begin to observe coseismic response on adjacent or even remote faults. A recent observation of such activity is the 2019 Ridgecrest seismic sequence that ruptured an unmapped fault of the Eastern California Shear Zone dextrally, and simultaneously triggered sinistral activity along the Garlock fault that strikes subperpendicular to the unmapped fault (Barnhart et al., 2019). If the triggered fault (in our case the Darvaz fault) is farther than a few fault lengths away from the main fault (in our case the Sarez-Karakul fault zone), Coulomb failure stress changes become insignificant (Tingay et al., 2008). Then, transient dynamic unclamping or triggering can be evoked by the surface waves passing through, as it has been observed on faults separated by up to 5 km (Freed, 2005). This is often the case along disconnected structures at immature fault systems (e.g., Gomberg, 1996). Another reason may be sudden pore pressure changes (Brodsky, 2003; Brodsky & Prejean, 2005). Significantly, the Darvaz fault (this study) and the Pamir thrust system (Metzger et al., 2018) slipped opposite to their loading sense, which would indicate that the coseismic mass movements outweigh the local stress field, even 150–200 km away from the epicenter of the Sarez earthquake in the southern Sarez-Karakul fault segment. In other words, the surface displacement predicted by the homogeneous half-space model of Metzger et al. (2017) (pink arrows in Figure 4) dominate the sense of displacement until they hit a structural discontinuity—the Darvaz fault or the evaporitic décollement underneath Peter the First Range—and then quickly drop below significance.

As we were not able to correct the 2016 campaign data for the (potential) coseismic displacement due to the Sarez earthquake, we omitted them for the interseismic slip rate estimates. The observed ~15 mm/yr sinistral slip across the Darvaz fault zone, measured on profile P1, is consistent with the 4–16 mm/yr of offset in the Holocene and Pleistocene (e.g., Burtman & Molnar, 1993). Farther south—along profile P2—we observed 8 $\pm$ 1 mm/yr sinistral shear, which is less than the 10–15 mm/yr offset measured by Trifonov, (1978, 1983). The GNSS data further suggest extension of ~10 mm/yr across the northern part of the Darvaz fault (profile P1),

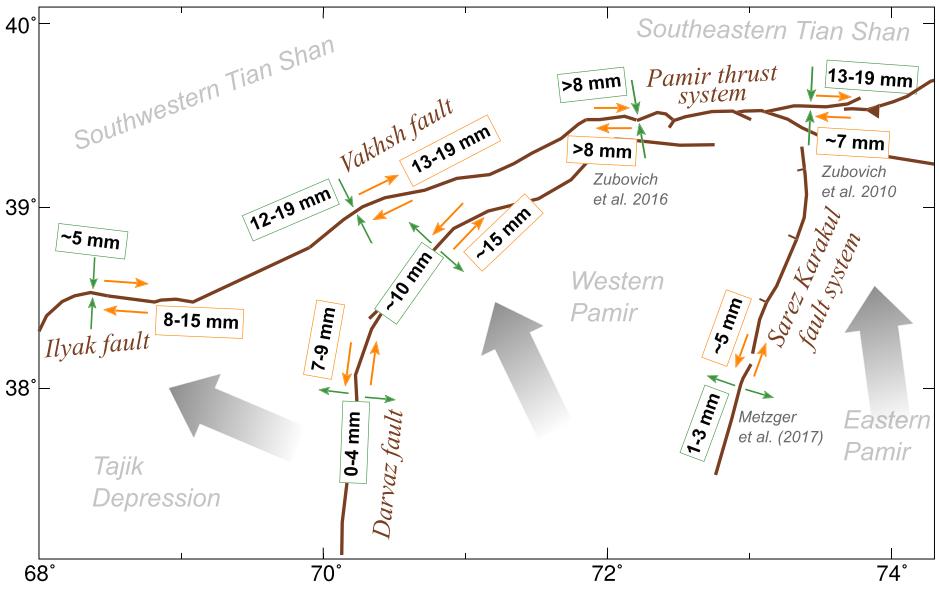

Figure 7. Same as Figure 1b, indicating the kinematics in the western Pamir and Tajik Depression. The gray arrows indicate the main direction of motion with respect to stable Eurasia observed by GNSS, the orange arrows indicate shear, the green arrows shortening or extension. The values are deducted from models and/or GNSS observations of Zubovich et al. (2010, 2016), Metzger et al. (2017), and this study. Rates of Zubovich et al. (2016) represent a lower limit, given the limited profile length toward south.

which has not been observed in neotectonic studies. Along the southern part of the Darvaz fault, geologic mapping indicated sinistral transtension (Kuchai & Trifonov, 1977; Trifonov, 1978, 1983), which corresponds to our GNSS results. No neotectonic slip rates are available for the Vakhsh fault. However, the geologic and geodetic findings agree on the slip sense.

While the sparse and widely distributed published GNSS rates (Ischuk et al., 2013; Mohadjer et al., 2010; Zhou et al., 2016) are in general agreement with our findings, the leveling results of Guseva (1986) and Konolpatsev (1971) acquired across the Vakhsh fault near Garm are systematically lower with 8–16 mm/yr shortening and ~6 mm/yr dextral shear, compared to our 12–19 mm/yr shortening and 13–19 mm/yr dextral shear. This might be explained by the shorter measurement profile and/or the possibility that their data were affected by postseismic deformation following the 1949, M_w7.6 Khait earthquake.

The seismicity along our GNSS Profile 1 (Figure 6a) shows significant, vertically aligned activity underneath Peter the First Range and along the Darvaz fault. This activity extends into the basement rocks underneath the evaporitic décollement, which is mimicked in our kinematic model by the Segments A and B. The updip end of Segment B ends just between these two highly active zones, probably because we have not included an additional (subvertical) segment to account for slip underneath Peter the First Range. Our model also likely underestimates the magnitude of the rate changes for the profile-parallel and profile-perpendicular GNSS components across the Vakhsh fault. This might be due to slip partitioning in the upper segment of the fault zone or even due to a three-dimensional rotation of the Peter the First Range that also includes vertical motions.

We combine our findings with other geodesy-based results (Zubovich et al., 2010, 2016; Metzger et al., 2017) to create a conceptual model for the northeastern Tajik Basin and the western and northern Pamir, highlighting the kinematics of the key structures, that is, the Vakhsh and Darvaz faults, the Pamir thrust system and the Sarez-Karakul fault system (Figure 7). The Pamir is shortening approximately N-S and is flowing westward at the same time, that is, experiencing lateral extrusion from the Pamir Plateau toward the Tajik Depression. In the Pamir interior this combined N-S shortening and E-W extension is mostly accommodated by the NE striking Sarez-Karakul fault system (Figure 1b), which interseismically exhibits ~5 mm/yr sinistral shear and 1–3 mm/yr of extension (see Figure S11 in Metzger et al., 2017); however, the entire western Pamir Plateau shows this deformation pattern. The due west motion of the Tajik

Depression upper crust commences west of the Darvaz fault zone, which shows sinistral shear of ~15 mm/yr and ~10 mm/yr E-W extension. Along the northwestern rim of Peter the First Range, the SE dipping Vakhsh fault separates the Tajik Depression from the southwestern Tian Shan; the latter marks the nearly rigid backstop for the material flow out of the Pamir Plateau. The Vakhsh fault absorbs dextral shear of 16 ±3 mm/yr and 15 + 4/−2 mm/yr of NW-SE shortening. Along the Ilyak fault farther west, N-S shortening drops to ~5 mm/yr but dextral shear remains high (8–15 mm/yr). On the Pamir thrust system farther east, dextral shortening (and thus Pamir-Plateau mass outflow) decreases to ~7 mm/yr, while the Pamir's northward advance keeps constant at a rate of 13–19 mm/yr (Zubovich et al., 2016, 2010). The Peter the First Range, an upper-crustal wedge of strongly shortened Tajik-basin strata squeezed between the Vakhsh and the Darvaz faults, extrudes as a southwestward widening crustal sliver. Although the lateral extrusion of the upper-crustal wedge is facilitated by the low-frictional properties of the evaporitic basal décollement, subdécollement seismicity indicates a thick-skinned sliver extrusion, demonstrated to be active within the adjacent Tian Shan from the late Miocene to Recent (Käßner et al., 2016).

6. Conclusion

New GNSS campaign data collected over 4 years (2013–2016) in the western Pamir and the adjacent Tajik Depression along two profiles crossing the Vakhsh and the Darvaz faults zone show steady interseismic motions from 2013-2015 and static offsets of up to 2 cm between the 2015 and the 2016 measurements, consistent with dextral fault slip on the Darvaz fault, opposite to its interseismic and long-term slip history. We propose that the 2015, M_w7.2 Sarez earthquake triggered the dextral movements along the Darvaz fault.

Velocities obtained from data prior to the 2016 observations show that the W(SW) striking Ilyak and Vakhsh faults and the Pamir thrust system constitute the highly active boundary zone between in the Pamir, the Tajik Depression, and the nearly stable foreland, the southwestern Tian Shan. From W to E, these structures accommodate shortening of ~5 mm/yr (Ilyak fault), 15 + 4/−2 mm/yr (Vakhsh fault), and 13–19 mm/yr (Pamir thrust system). Dextral shear rates are high at the northern edge of the Tajik Depression (8–15 mm/yr along the Ilyak fault; 16 ±3 mm/yr along the Vakhsh fault) but decrease eastward to ~7 mm/yr along the Pamir thrust system. For the Darvaz fault we obtained 10–15 mm/yr sinistral slip and ~10 mm/yr of approximately E-W extension. We further surmise that the Pamir Plateau and the hanging wall of the Vakhsh thrust in the Peter the First Range are still growing vertically by a few millimeters per year, while the Tajik Depression is subsiding.

Our geodetic data indicate, in accordance with the geologic and seismic record that the eastern Tajik Depression, including the Peter the First Range, is collapsing (lateral extruding) toward the west. The southwestern Tian Shan acts as a backstop and deforms little. The gravity-driven mass-outflow from the Pamir Plateau to its west induces shortening of the Tajik-basin deposits, forming the Tajik-basin fold-thrust belt, facilitated by the near-horizontal, evaporitic basal décollement of the fold-thrust belt. The Ilyak fault marks a major tear fault, disconnecting the shortening in the Tajik basin fold-thrust belt from the weakly deforming Tian Shan backstop. Thus, combining the geodetic results with the geologic and thermochronologic constraints from the Pamir Plateau, Tajik Basin, and Tian Shan foreland, it appears that northward displacement and westward lateral extrusion of the Pamir Plateau into the Tajik Depression have been active since the late Miocene.

Acknowledgments
We thank Zukhra Ilyasova, Akram Akhmedov, and Shorukh Murodkulov for helping us collecting the GNSS data. The GNSS RNX files are published via GFZ Data Services (Metzger et al., 2019). Some figures were produced using the Generic Mapping Tools (GMT) public domain software (Wessel et al., 2013). We thank Richard Walker an anonymous reviewer for their valuable comments.

References

Altamimi, Z., Métivier, L., & Collilieux, X. (2012). ITRF2008 plate motion model. *Journal of Geophysical Research*, *117*, 1–14. https://doi.org/10.1029/2011JB008930

Altamimi, Z., Métivier, L., Rebischung, P., Rouby, H., & Collilieux, X. (2017). ITRF2014 plate motion model. *Geophysical Journal International*, *209*(3), 1906–1912. https://doi.org/10.1093/gji/ggx136

Altamimi, Z., Rebischung, P., Métivier, L., & Collilieux, X. (2016). ITRF2014: A new release of the International Terrestrial Reference Frame modeling nonlinear station motions. *Journal of Geophysical Research: Solid Earth*, *121*, 6109–6131. https://doi.org/10.1002/2016JB013098

Babaev, A. M. (1975). *Recent tectonics of the zone of orogenesis of the Gissar-Alai and Tajik Depression* (p. 149). Dushanbe: Donish (in Russian).

Barnhart, W. D., Hayes, G. P., & Gold, R. D. (2019). The July 2019 Ridgecrest, California earthquake sequence: Kinematics of slip and stressing in cross fault ruptures. *Geophysical Research Letters*, *46*, 11,859–11,867. https://doi.org/10.1029/2019gl084741

Bodin, P., Bilham, R., Behr, J., Gomberg, J., & Hudnut, K. W. (1994). Slip triggered on southern California faults by the 1992 Joshua Tree, Landers, and Big Bear earthquakes. *Bulletin of the Seismological Society of America*, *84*(3), 806–816. https://doi.org/10.1016/0148-9062(95)94487-7

Bourgeois, O., Cobbold, P. R., Rouby, D., Thomas, J.-C. J., & Shein, V. (1997). Least squares restoration of Tertiary thrust sheets in map view, Tajik depression, central Asia. *Journal of Geophysical Research*, *102*(B12), 27,553–27,573. https://doi.org/10.1029/97JB02477

Brodsky, E. E. (2003). A mechanism for sustained groundwater pressure changes induced by distant earthquakes. *Journal of Geophysical Research*, *108*(B8), 1–10. https://doi.org/10.1029/2002jb002321

Brodsky, E. E., & Prejean, S. G. (2005). New constraints on mechanisms of remotely triggered seismicity at Long Valley Caldera. *Journal of Geophysical Research*, *110*, 1–14. https://doi.org/10.1029/2004JB003211

Burtman, V. S., & Molnar, P. (1993). Geological and geophysical evidence for deep subduction of continental crust beneath the Pamir. *Geological Society of America, Special Paper*, *281*, 1–76.

Cervelli, P., Murray, H. M., Segall, P., Aoki, Y., & Kato, T. (2001). Estimating source parameters from deformation data, with an application to the March 1997 earthquake swarm off the Izu Peninsula. *Journal of Geophysical Research*, *106*(B6), 11,217–11,237. https://doi.org/10.1029/2000JB900399

Chapman, J. B., Carrapa, B., Ballato, P., DeCelles, P. G., Worthington, J., Oimahmadov, I., et al. (2017). Intracontinental subduction beneath the Pamir Mountains: Constraints from thermokinematic modeling of shortening in the Tajik fold-and-thrust belt. *GSA Bulletin*, *129*(11–12), 1450–1471. https://doi.org/10.1130/B31730.1

Chen, J., Schoenbohm, L. M., Yuan, Z., Li, W., Li, T., Owen, L. A., et al. (2011). Holocene slip rate along the northern Kongur extensional system, Chinese Pamir. *AGU Fall Meeting*, T43F–T2447F.

Chevalier, M. L., Pan, J., Li, H., Liu, D., & Wang, M. (2015). Quantification of both normal and right-lateral late Quaternary activity along the Kongur Shan extensional system, Chinese Pamir. *Terra Nova*, *27*(5), 379–391. https://doi.org/10.1111/ter.12170

DeMets, C., Gordon, R. G., Argus, D. F., & Stein, S. (2010). Geologically current plate motions. *Geophysical Journal International*, *181*(1), 1–80. https://doi.org/10.1111/j.1365-246X.2009.04491.x

Deng, Z., Gendt, G., & Schöne, T. (2016). Status of the IGS-TIGA tide gauge data reprocessing at GFZ. *International Association of Geodesy Symposia*, (January 1994, 33–40. https://doi.org/10.1007/1345_2015_156

Dong, D., Fang, P., Bock, Y., Cheng, M. K., & Miyazaki, S. (2002). Anatomy of apparent seasonal variations from GPS-derived site position time series. *Journal of Geophysical Research*, *107*(B4), ETG 9-1–ETG 9-16. https://doi.org/10.1029/2001JB000573

Dooley, T. P., Jackson, M. P. A., & Hudec, M. R. (2015). Breakout of squeezed stocks: Dispersal of roof fragments, source of extrusive salt and interaction with regional thrust faults. *Basin Research*, *27*(1), 3–25. https://doi.org/10.1111/bre.12056

Dziewonski, A. M., Chou, T.-A., & Woodhouse, J. H. (1981). Determination of earthquake source parameters from waveform data for studies of global and regional seismicity. *Journal of Geophysical Research*, *86*, 2825–2852. https://doi.org/10.1029/JB086iB04p02825

Efron, B. (1979). Bootstrap methods: Another look at the Jackknife. *The Annals of Statistics*, *7*(1), 1–26. https://doi.org/10.1214/aos/1176344552

Ekström, G., Nettles, M., & Dziewonski, A. M. (2012). The global CMT project 2004–2010: Centroid-moment tensors for 13,017 earthquakes. *Physics of the Earth and Planetary Interiors*, *200-201*, 1–9. https://doi.org/10.1016/j.pepi.2012.04.002

Engdahl, E. R., van der Hilst, R., & Buland, R. (1998). Global teleseismic earthquake relocation with improved travel times and procedures for depth determination. *Bulletin of the Seismological Society of America*, *88*, 722–743.

Evans, S. G., Roberts, N. J., Ischuk, A., Delaney, K. B., Morozova, G. S., & Tutubalina, O. (2009). Landslides triggered by the 1949 Khait earthquake, Tajikistan, and associated loss of life. *Engineering Geology*, *109*, 195–212. https://doi.org/10.1016/j.enggeo.2009.08.007

Fan, G., Ni, J. F., & Wallace, T. C. (1994). Active tectonics of the Pamirs and Karakorum. *Journal of Geophysical Research*, *99*(B4), 7131–7160.

Freed, A. M. (2005). Earthquake triggering by static, dynamic, and postseismic stress transfer. *Annual Reviews of Earth and Planetary Science*, *33*, 335–367. https://doi.org/10.1146/annurev.earth.33.092203.122505

Geirsson, H., Árnadóttir, T., Völksen, C., Jiang, W., Sturkell, E., Villemin, T., et al. (2006). Current plate movements across the Mid-Atlantic ridge determined from 5 years of continuous GPS measurements in Iceland. *Journal of Geophysical Research*, *111*, B09407. https://doi.org/10.1029/2005JB003717

Gendt, G., Deng, Z., Ge, M., Nischan, T., Uhlemann, M., Beeskov, G., et al. (2013). GFZ analysis center of IGS - Annual report for 2013. Retrieved from ftp://ftp.gfz-potsdam.de/GNSS/DOCS/IGS_repro2/GFZ_igs_annual_report_2013_iss1-0.pdf (last accessed date: Jan 29, 2020).

GEOFON Data Centre. (1993). GEOFON Seismic Network. Deutsches GeoForschungsZentrum GFZ. https://doi.org/10.14470/TR560404

Gomberg, J. (1996). Stress/strain changes and triggered seismicity following the M_w7.3 Landers, California earthquake. *Journal of Geophysical Research*, *101*, 751–764. https://doi.org/10.1029/95JB03251

Guseva, T. G. (1986). Contemporary movements of the Earth's crust in the transition zone from the Pamir to the Tian Shan (in Russian), Moscow Institute of Physics of the Earth. Academi Nauk, 171.

Hamburger, M. W., Sarewitz, D. R., Pavlis, T. L., & Popandopulo, G. A. (1992). Structural and seismic evidence for intracontinental subduction in the Peter the First Range, Central Asia. *Geological Society of America Bulletin*, *104*, 397–408.

Herring, T. A., Floyd, M. A., King, R. W., & McClusky, S. C. (2015). GLOBK reference manual, Release 10.6, Technical Report, Department of Earth, Atmospheric, and Planetary Sciences, Massachusetts Institute of Technology.

Herring, T. A., King, R. W., Floyd, M. A., & McClusky, S. C. (2018a). Introduction to GAMIT/GLOBK, Release 10.7, Technical Report, Department of Earth, Atmospheric, and Planetary Sciences, Massachusetts Institute of Technology.

Herring, T. A., King, R. W., Floyd, M. A., & McClusky, S. C. (2018b). GAMIT reference manual, release 10.7, Technical Report, Department of Earth, Atmospheric, and Planetary Sciences, Massachusetts Institute of Technology.

Ischuk, A., Bendick, R., Rybin, A., Molnar, P., Khan, S. F., Kuzikov, S., et al. (2013). Kinematics of the Pamir and Hindu Kush regions from GPS geodesy. *Journal of Geophysical Research: Solid Earth*, *118*, 2408–2416. https://doi.org/10.1002/jgrb.50185

Käßner, A., Ratschbacher, L., Jonckheere, R., Enkelmann, E., Khan, J., Sonntag, B.-L., et al. (2016). Cenozoic intracontinental deformation and exhumation at the northwestern tip of the India-Asia collision—southwestern Tian Shan, Tajikistan, and Kyrgyzstan. *Tectonics*, *35*, 2171–2194. https://doi.org/10.1002/2015TC003897

Kondorskaya, N., & Shebalin, N. (chief editors). (1982). New catalog of strong earthquakes in the U.S.S.R. from ancient times through 1977. Report SE31, World Data Center A for Solid Earth Geophysics, 609. https://doi.org/ftp://ftp.ngdc.noaa.gov/hazards/publications/Wdcse-31.pdf

Konolpatsev, I. M. (1971). Measurements of crustal movements in the Garm area, 1948-1970 (in Russian). *Geotektonika*, *5*, 111–116.

Kuchai, V., & Trifonov, V. (1977). Young left-lateral strike-slip along the zone of the Darvaz Fault (in Russian). *Geotektonika*, *3*, 91–105.

Kufner, S.-K., Schurr, B., Ratschbacher, L., Murodkulov, S., Abdulhameed, S., Ischuk, A., et al. (2018). Seismotectonics of the Tajik Basin and surrounding Mountain Ranges. *Tectonics*, *37*, 2404–2424. https://doi.org/10.1029/2017tc004812

Kufner, S.-K., Schurr, B., Sippl, C., Yuan, X., Ratschbacher, L., Ischuk, A., et al. (2016). Deep India meets deep Asia: Lithospheric indentation, delamination and break-off under Pamir and Hindu Kush (Central Asia). *Earth and Planetary Science Letters*, *435*, 171–184. https://doi.org/10.1016/j.epsl.2015.11.046

Kulikova, G. (2016). Source parameters of the major historical earthquakes in the Tien-Shan region from the late 19th to the early 20th century. PhD Thesis. Potsdam University.

Kulikova, G., Schurr, B., Krüger, F., Brzoska, E., & Heimann, S. (2015). Source parameters of the Sarez-Pamir earthquake of 1911 February 18. *Geophysical Journal International*, *205*(2), 1086–1098. https://doi.org/10.1093/gji/ggw069

Legler, B. A., & Przhiyalgovskaya, I. A. (1979). *The interaction of the Indian and Asian lithospheric plates and the tectonics of the Tadjik Depression (in Russian) In: Structure of lithospheric plates* (pp. 125–188). Akademi Nauk, USSR, Moscow: Institute of Oceanology.

Leith, W., & Alvarez, W. (1985). Structure of the Vakhsh fold-and-thrust belt, Tadjik SSR: Geologic mapping on a Landsat image base. *Bulletin of the Geological Society of America*, *96*(7), 875–885. https://doi.org/10.1130/0016-7606(1985)96<875:SOTVFB>2.0.CO;2

Leith, W., & Simpson, D. W. (1986). Earthquakes related to active salt doming near Kulyab, Tadjikistan, USSR. *Geophysical Research Letters*, *13*(10), 1019–1022. https://doi.org/10.1029/GL013i010p01019

Liu, Q. (1993). Paleoclimat et contraintes chronologiques sur les mouvements recent dans l'Ouest du Tibet: Failles du Karakorum et de Longmu Co–Gozha Co, lacs en pull-apart de Longmu Co et de Sumxi Co. PhD Thesis. Universite Paris VII.

Lyard, F., Lefevre, F., Letellier, T., & Francis, O. (2006). Modelling the global ocean tides: Modern insights from FES2004. *Ocean Dynamics*, *56*(5–6), 394–415. https://doi.org/10.1007/s10236-006-0086-x

Mai, M. P., & Beroza, G. C. (2000). Source scaling properties from finite-fault-rupture models. *Bulletin of the Seismological Society of America*, *90*(3), 604–615. https://doi.org/10.1785/0119990126

Metzger, S., Ischuk, A., Akhmedov, A., Ilyasova, Z., Moreno, M., Murodkulov, S., & Deng, Z. (2019). Survey mode GPS data in the West Pamir, Tajikistan, Central Asia, 2013–2016. *GFZ Data Services*. https://doi.org/10.5880/GFZ.4.1.2019.007

Metzger, S., Ischuk, A., Zubovich, A., Deng, Z., Schöne, T., Schurr, B., et al. (2018). Observations from four high-resolution GPS profiles across the active margin of the Pamir, Central Asia: Can we discriminate interseismic fault-slip rates, slip partitioning, and even co-seismically triggered slip? *Geophysical Research Abstracts*, *20*, EGU2018-16410–1.

Metzger, S., Schurr, B., Ratschbacher, L., Sudhaus, H., Kufner, S.-K., Schöne, T., et al. (2017). The 2015 M_w7.2 Sarez strike-slip earthquake in the Pamir interior: Response to the underthrusting of India's western promontory. *Tectonics*, *36*, 2407–2421. https://doi.org/10.1002/2017TC004581R

Mohadjer, S., Bendick, S. R., Ischuk, A., Kuzikov, S., Kostuk, A., Saydullaev, U., et al. (2010). Partitioning of India/Eurasia convergence in the Pamir-Hindu Kush from GPS measurements. *Geophysical Research Letters*, *37*. https://doi.org/10.1029/2009GL041737

Nikolaev, V. G. (2002). Afghan-Tajik depression: Architecture of sedimentary cover and evolution. *Russian Journal of Earth Sciences*, *4*(6), 399–421.

Nikonov, A. A. (1970). Differential analysis of the Quaternary tectonics of the Afghan-Tadjik Depression (in Russian). *Geotektonika*, *1*, 101–107.

Nikonov, A. A. (1975). An analysis of tectonic movements along the Hindu Kush-Darvaz-Karakul fault zone in late Pliocene and Quaternary time (in Russian). Bulletin MOIP (of the Moscow Society for the Investigation of Nature). *Geology Section*, *50*, 5–23.

Nikonov, A. A. (1977). *Holocene and contemporary movements of the earth's crust (in Russian)* (p. 240). Moscow: Nauka.

Okada, Y. (1985). Surface deformation due to shear and tensile faults in a half-space. *Bulletin of the Seismological Society of America*, *75*(4), 1135–1154. https://doi.org/10.1016/0148-9062(86)90674-1

Price, E. J., & Sandwell, D. T. (1998). Small-scale deformations associated with the 1992 Landers, California, earthquake mapped by synthetic aperture radar interferometry phase gradients. *Journal of Geophysical Research*, *103*(B11), 27,001–27,016. https://doi.org/10.1029/98jb01821

Ratschbacher, L., Merle, O., Davy, P., & Cobbold, P. (1991). Lateral extrusion in the Eastern Alps, Part 1: Boundary conditions and experiments scaled for gravity. *Tectonics*, *10*(2), 245–256.

Rebischung, P., Altamimi, Z., Ray, J., & Garayt, B. (2016). The IGS contribution to ITRF2014. *Journal of Geodesy*, *90*(7), 611–630. https://doi.org/10.1007/s00190-016-0897-6

Robert, A. M. M., Fernàndez, M., Jiménez-Munt, I., & Vergés, J. (2017). Lithospheric structure in Central Eurasia derived from elevation, geoid anomaly and thermal analysis. *Geological Society, London, Special Publications*, *427*(1), 271–293. https://doi.org/10.1144/SP427.10

Rutte, D., Ratschbacher, L., Schneider, S., Stübner, K., Stearns, M. A., Gulzar, M. A., & Hacker, B. R. (2017). Building the Pamir-Tibetan Plateau—Crustal stacking, extensional collapse, and lateral extrusion in the Central Pamir: 1. Geometry and kinematics. *Tectonics*, *36*, 342–384. https://doi.org/10.1002/2016TC004293

Ruzhentsev, S. V. (1963). Strike-slip faults of the southeastern Pamir (in Russian) In: Faults and horizontal movements of the Earth's crust. *Moscow, Nauka, Trudy Geological Institute, Akademi Nauk, USSR*, *80*, 113–127.

Ruzhentsev, S. V. (1968). *Tectonic development of the southeastern Pamir and the role of horizontal movements in the formation of its Alpine structure (in Russian)* (p. 202). Moscow: Nauka.

Sangha, S., Peltzer, G., Zhang, A., Meng, L., Lian, C., Lundgren, P., & Fielding, E. (2017). Fault geometry of 2015, M_w7.2 Murghab, Tajikistan earthquake controls rupture propagation: Insights from InSAR and seismological data. *Earth and Planetary Science Letters*, *462*, 132–141. https://doi.org/https://doi.org/10.1016/j.epsl.2017.01.018

Schmid, R., Dach, R., Collilieux, X., Jäggi, A., Schmitz, M., & Dilssner, F. (2016). Absolute IGS antenna phase center model igs08. atx: Status and potential improvements. *Journal of Geodesy*, *90*(4), 343–364. https://doi.org/10.1007/s00190-015-0876-3

Schneider, F. M., Yuan, X., Schurr, B., Mechie, J., Sippl, C., Haberland, C., et al. (2013). Seismic imaging of subducting continental lower crust beneath the Pamir. *Earth and Planetary Science Letters*, *375*, 101–112. https://doi.org/10.1016/j.epsl.2013.05.015

Schurr, B., Ratschbacher, L., Sippl, C., Gloaguen, R., Yuan, X., & Mechie, J. (2014). Seismotectonics of the Pamir. *Tectonics*, *33*, 1501–1518. https://doi.org/10.1002/2014TC003576

Segall, P. (2010). *Earthquake and volcano deformation*. Princeton: Princeton University Press. https://doi.org/10.1515/9781400833856

Sippl, C., Ratschbacher, L., Schurr, B., Krumbiegel, C., Rui, H., Pingren, L., & Abdybachaev, U. (2014). The 2008 Nura earthquake sequence at the Pamir-Tian Shan collision zone, southern Kyrgyzstan. *Tectonics*, *33*, 2382–2399. https://doi.org/10.1002/2014TC003705

Sippl, C., Schurr, B., Tympel, J., Angiboust, S., Mechie, J., Yuan, X., et al. (2013). Deep burial of Asian continental crust beneath the Pamir imaged with local earthquake tomography. *Earth and Planetary Science Letters*, *384*, 165–177. https://doi.org/10.1016/j.epsl.2013.10.013

Sippl, C., Schurr, B., Yuan, X., Mechie, J., Schneider, F. M., Gadoev, M., et al. (2013). Geometry of the Pamir-Hindu Kush intermediate-depth earthquake zone from local seismic data. *Journal of Geophysical Research: Solid Earth*, *118*, 1438–1457. https://doi.org/10.1002/jgrb.50128

Skobelev, S. F., & Florenskiy, P. V. (1974). Holocene tectonic deformation and rock slides in the Vakhsh overthrust zone. *Geotectonics*, *5*, 316–317.

Sridevi, J., Bhatt, B. C., Yang, Z., Bendick, R., Gaur, V. K., Molnar, P., et al. (2004). GPS measurements from the Ladakh Himalaya, India: Preliminary tests of plate-like or continuous deformation in Tibet. *GSA Bulletin*, *116*(11–12), 1385–1391. https://doi.org/10.1130/B25357.1

Storchak, D. A., Di Giacomo, D., Bondár, I., Engdahl, E. R., Harris, J., Lee, W. H. K., et al. (2013). Public release of the ISC-GEM global instrumental earthquake catalogue (1900-2009). *Seismological Research Letters*, *84*(5), 810–815. https://doi.org/10.1785/0220130034

Strecker, M. R., Frisch, W., Hamburger, M. W., Ratschbacher, L., Semiletkin, S., Zamoruyev, A., & Sturchio, N. (1995). Quaternary deformation in the eastern Pamirs, Tadzhikistan and Kyrgyzstan. *Tectonics*, *14*(5), 1061–1079. https://doi.org/10.1029/95TC00927

Stübner, K., Ratschbacher, L., Rutte, D., Stanek, K., Minaev, V., Wiesinger, R., Gloaguen, R., & Project TIPAGE members (2013). The giant Shakhdara migmatitic gneiss dome, Pamir, India-Asia collision zone, 1: Geometry and kinematics. *Tectonics*, *32*, 948–979. https://doi.org/10.1002/tect.20057

Tingay, M., Heidbach, O., Davies, R., & Swarbrick, R. (2008). Triggering of the Lusi mud eruption: Earthquake versus drilling initiation. *Geology*, *36*(8), 639–642. https://doi.org/10.1130/G24697A.1

Trifonov, V. (1978). Late Quaternary tectonic movements of western and central Asia. *Bulletin of the Geological Society of America*, *89*(7), 1059–1072.

Trifonov, V. (1983). Late Quaternary tectogenesis (in Russian): Moscow. *Nauka*, 224.

USGS. (2015). M 7.2-104 km W of Murghob, Tajikistan.

Victor, P., Oncken, O., Sobiesiak, M., Kemter, M., Gonzalez, G., & Ziegenhagen, T. (2018). Dynamic triggering of shallow slip on forearc faults constrained by monitoring surface displacement with the IPOC Creepmeter Array. *Earth and Planetary Science Letters*, *502*, 57–73. https://doi.org/10.1016/j.epsl.2018.08.046

Wei, M., Sandwell, D., Fialko, Y., & Bilham, R. (2011). Slip on faults in the Imperial Valley triggered by the 4 April 2010 M_w7.2 El Mayor-Cucapah earthquake revealed by InSAR. *Geophysical Research Letters*, *38*, 1–6. https://doi.org/10.1029/2010GL045235

Wessel, P., Smith, W. H. F., Scharroo, R., Luis, J. F., & Wobbe, F. (2013). Generic mapping tools: Improved version released. *Eos, Transactions American Geophysical Union*, *94*, 409–410. https://doi.org/10.1002/2013EO450001

Worthington, J. R., Ratschbacher, L., Stübner, K., Khan, J., Malz, N., Schneider, S., et al. (2019). The Alichur dome, South Pamir, western India–Asia collisional zone: Detailing the Neogene Shakhdara–Alichur syn-collisional gneiss-dome complex and connection to lithospheric processes. *Tectonics*, *39*. https://doi.org/10.1029/2019TC005735

Wright, T., Fielding, E. J., & Parsons, B. (2001). Triggered slip: Observations of the 17 August 1999 Izmit (Turkey) earthquake using radar interferometry. *Geophysical Research Letters*, *28*(6), 1079–1082. https://doi.org/10.1029/2000GL011776

Zakharov, S. A. (1948). On the east-west strike-slip faults on the south front of the Gissar Range (in Russian). *Reports of the Tadjik Filial Akademi Nauk of the USSR*, *5*, 3–5.

Zakharov, S. A. (1955). On the relationship of the Tadjik Depression and the Gissar Range (in Russian). *Izvestiya, Branch of Natural Sciences of the Tadjik SSR*, *9*, 15–20.

Zakharov, S. A. (1958). *Sediment structure of the Mesozoic and Cenozoic of the Tadjik Depression (in Russian)* (p. 230). Donish: Stalinabad.

Zhou, Y., He, J., Oimahmadov, I., Gadoev, M., Pan, Z., Wang, W., et al. (2016). Present-day crustal motion around the Pamir Plateau from GPS measurements. *Gondwana Research*, *35*, 144–154. https://doi.org/10.1016/j.gr.2016.03.011

Zubovich, A., Schöne, T., Metzger, S., Mosienko, O., Mukhamediev, S., Sharshebaev, A., & Zech, C. (2016). Tectonic interaction between the Pamir and Tien Shan observed by GPS. *Tectonics*, *35*, 283–292. https://doi.org/10.1002/2015TC004055

Zubovich, A. V., Wang, X., Scherba, Y. G., Schelochkov, G. G., Reilinger, R., Reigber, C., et al. (2010). GPS velocity field of the Tien Shan and surrounding regions. *Tectonics*, *29*, TC6014. https://doi.org/10.1029/2010TC002772